OSMA/MEO/Report–13

The Activity Profiles and Peak Flux of Radar Meteor Showers

A. V. Moorhead
Marshall Space Flight Center, Huntsville, Alabama

M. D. Campbell-Brown and P. G. Brown
Department of Physics and Astronomy, University of Western Ontario, London, Ontario

Abstract: Meteor showers are transient phenomena; a limited duration is what distinguishes a shower from a sporadic source. They do not, however, have clear start and end times; instead, shower activity gradually (or rapidly) increases over time, reaches a peak, and then decays. In this report, we examine the activity profiles of 38 meteor showers using 20 years of single-station shower fluxes from the Canadian Meteor Orbit Radar (CMOR). We find that a number of showers, such as the Southern delta Aquariids (SDAs), exhibit a broad maximum in activity rather than a sharp peak. We also find that approximately one-third of showers exhibit asymmetric activity profiles in which the rate in which activity rises prior to the peak differs from the rate at which it decays after the peak. We provide a functional form for meteor shower activity profiles that incorporates these features and use these profile fits to estimate each shower's peak flux.

This report also includes an uncertainty analysis for CMOR fluxes. This includes the first (to our knowledge) characterization of systematic uncertainty in radar meteor fluxes.

April 2024 Report

TABLE OF CONTENTS

LIST OF FIGURES

LIST OF TABLES

LIST OF ACRONYMS

CDF	cumulative distribution function
CMOR	Canadian Meteor Orbit Radar
FWHM	full width at half maximum
GLD4	type IV generalized logistic distribution
PDF	probability distribution function

LIST OF METEOR SHOWER ABBREVIATIONS

AHY	alpha Hydrid
AND	Andromedid
ARI	Daytime Arietid
AUM	alpha Ursae Majorid
BEQ	beta Equuleid
CAP	alpha Capricornid
DRA	October Draconid
DSX	Daytime Sextantid
ETA	eta Aquariid
GEM	Geminid
GUM	gamma Ursae Minorid
LBO	lambda Boötid
LEO	Leonid
LYR	April Lyrid
NID	November iota Draconid
NZC	Northern June Aquilid
OCE	Southern Daytime omega Cetid
ORI	Orionid
PER	Perseid
QUA	Quadrantid
SDA	Southern delta Aquariid
SSE	sigma Serpentid
SZC	Southern June Aquilid
TCB	theta Coronae Borealid
URS	Ursid
XCB	xi Coronae Borealid
XDR	xi Draconid
ZPE	Daytime zeta Perseid

NOMENCLATURE

${}_2F_1$	ordinary or Gauss hypergeometric function
α	confidence level
χ^2	chi-squared statistic
χ^2_{mod}	modified chi-squared statistic
γ	background contamination fraction
γ_0	highest plausible background contamination fraction
λ_0	solar longitude of shower peak
$\lambda_\odot$	solar longitude
ν	degrees of freedom
σ_y	standard deviation of the fit residuals
$\hat{\sigma}_y$	estimated standard deviation of the residuals
$\hat{\sigma}_{\ln f}$	estimated standard deviation in $\ln f$
a	rate of exponential growth before peak
b	rate of exponential decay after peak
B	complete beta function
B^+	rate of 10-fold growth before peak
B^-	rate of 10-fold decay after peak
c	smoothing parameter
f	flux
f_{29}	experimental pipeline flux for 29 MHz data
f_{38}	experimental pipeline flux for 38 MHz data
f_{op}	operational pipeline flux for 29 MHz data
f_i	i^{th} flux measurement
$\bar{f}_j$	mean flux in solar longitude bin j
G	functional form of CDF
g	functional form of PDF
G_{bg}	CDF for sporadic background contamination
g_{bg}	PDF for sporadic background contamination
g_{tot}	PDF for all meteors (shower and background)
G_{trunc}	truncated form of a CDF
g_{trunc}	truncated form of a PDF
k	activity profile steepness parameter
ℓ	activity profile asymmetry parameter
m	slope of background contamination
m_j	number of flux measurements in bin j
n	number of meteors
n_{par}	number of fit parameters
s_i	estimated error in flux measurement i
s_j	standard deviation of flux in solar longitude bin j
t^*	t-statistic
t_{crit}	maximum t-statistic for non-outlying data points
v_{atm}	in-atmosphere speed of a meteor shower

w_j	solar longitude weighting factor
y_i	i^{th} scaled flux measurement
$\bar{y}_j$	mean scaled flux in solar longitude bin j
expit	standard logistic function
ZHR	zenithal hourly rate
ZHR_0	peak zenithal hourly rate

THE ACTIVITY PROFILES AND PEAK FLUX OF RADAR METEOR SHOWERS

1 Introduction

The most basic observable properties of a meteor shower are the radiant, speed, and time at which activity peaks: these quantities define the stream's trajectory as it intersects the Earth and therefore also its orbit. However, these four quantities describe only the mean shower trajectory at the time of the peak. The meteors belonging to a given shower will possess a distribution of radiants, speeds, and solar longitudes; for instance, meteor radiants appear to follow a Rayleigh distribution (Moorhead et al., 2021), and solar longitudes tend to follow an asymmetric Laplace distribution (Jenniskens, 1994).

The duration or pattern of a shower's activity is – like radiant, speed, or timing – a useful point of comparison for additional observations or studies. For instance, one can test whether a shower's activity in subsequent years follows the same pattern. When activity differs, having a model for the typical solar longitude distribution can lead to a better characterization of outbursts. The temporal distribution itself can also place an important constraint on dynamical models (see, e.g., Egal et al., 2020). Our own motivation is to carefully measure the peak flux in order to assess shower relevance compared to the sporadic background.

Meteor shower durations are often described qualitatively, especially for newly discovered and typically "brief" showers. Quantitative measures of duration are much less common, and typically take one of two forms. In the first, the observer describes the "start" and "end" of detectable activity (examples include Cook, 1973; Brown et al., 2008; SonotaCo, 2009; Molau and Rendtel, 2009; Jenniskens et al., 2016). A second, less common measure of meteor shower duration is the full width at half maximum (FWHM; examples include Cook, 1973; Younger et al., 2015; Ogawa and Steyaert, 2017; Molau et al., 2019; Jenniskens et al., 2020). Both measures have have limitations. Meteoroid streams typically contain a larger proportion of large meteoroids than the sporadic complex, and appear more significant when observed at larger sizes/brighter magnitudes. As a result, the shower may be detectable over the sporadic background for a shorter period of time when viewed by a network sensitive to small meteoroids. Indeed, the Brown et al. (2008) survey, which is based on radar observations of meteors with magnitudes between +5 and +9, reports significantly shorter durations for many showers than the SonotaCo (2009) and Jenniskens et al. (2016) video surveys, which detect meteors with magnitudes between -2 and +4. The FWHM is a more useful quantity to compare with meteoroid stream models. On the other hand, it is less useful for predicting when a shower is detectable by observers or hazardous to spacecraft.

A complete description of the activity profile, on the other hand, can be used to predict the interval within which a shower exceeds any desired observability threshold. Jenniskens (1994) demonstrated that the activity profiles of many showers are well-represented by a double exponential (or Laplace distribution; see section 4.1). Some showers, such as the Geminids (GEMs), showed strong signs of asymmetry. A handful of showers – including the GEMs, Leonids (LEOs),

Perseids (PERs), and Ursids (URSs) – required a superposition of two different double exponential profiles to recreate their activity profile. These profiles and their parameters have now been used to predict the meteor shower activity encountered by spacecraft for over 25 years (McBride, 1997; Moorhead et al., 2017; Moorhead et al., 2019).

While many of the Jenniskens (1994) profiles continue to be a good match for observed activity, others were based on data with a low signal-to-noise ratio. The Daytime Arietids (ARIs), for instance, have a fairly noisy profile. Additionally, these profiles are based on visual meteor counts and thus radar and daytime showers are not represented (the "Daytime" Arietids are an exception, as they occur around dawn and produce a few nighttime meteors). Furthermore, years of meteoroid flux data have been collected in the intervening decades. The time is ripe to reexamine the form of meteor shower activity profiles, refine fits to existing showers, and expand our fitting procedures to new showers.

In this paper, we fit activity profiles using 20 years of meteor flux data from the Canadian Meteor Orbit Radar (CMOR; Jones et al., 2005; Campbell-Brown, 2004). We obtained profile shape parameters for 38 meteor showers, many of which are only visible via radar. We find that about half of these showers are better fit by a generalized logistic distribution with a more rounded peak, described in section 4.2. In all cases, we incorporate sporadic contamination into our fitting algorithm; if sporadic contamination is neglected, the peak flux may be severely overestimated.

2 Meteor flux measurements

Three radar transmitters are located at CMOR's central site and emit at different frequencies: 17.45, 29.85, and 38.15 MHz. The main site has a set of receivers corresponding to each frequency. 29 MHz receivers are also located at five remote sites (Webster et al., 2004; Jones et al., 2005; Brown and Weryk, 2020). If the reflection of the radar pulse off a meteor trail is detected by receivers at multiple sites, it is possible to derive a trajectory and obtain the meteor's radiant and speed. These multi-station data are used to survey shower activity (e.g., Brown et al., 2008, 2010), among other applications.

CMOR also collects single-station observations using all three frequencies. Single-station data are preferred for meteor flux calculations because accounting for observing biases is simpler (Campbell-Brown, 2004). On the other hand, single-station data lack radiant and speed information, making it difficult to discriminate between shower members and non-shower members.[1] The only shower membership diagnostic, other than timing, is the angular distance between the shower radiant, radar station, and meteor at the time of detection (Jones and Morton, 1977). As a result, the shower fluxes will be more contaminated by sporadics than the multi-station shower survey data. Accounting for this contamination will be an important component of our activity characterization (see section 4.5).

CMOR also has two different flux pipelines; an "operational" pipeline that has been in place, unchanged, since 2002, and an "experimental" pipeline. The experimental pipeline offers additional options, such as the ability to exclude competing showers, and incorporates improvements,

[1] While speed estimates can be generated for single-station observations of meteors using the "pre-t0 method" (Cervera et al., 1997), this method does not work well for the small meteoroids that dominate our flux measurements.

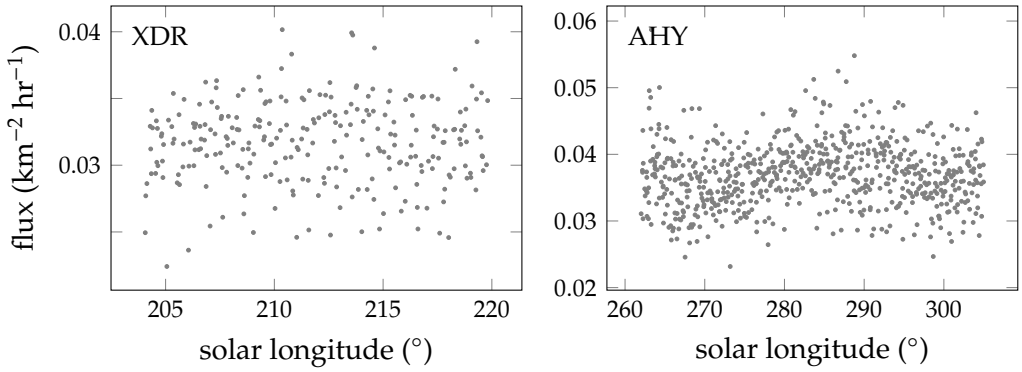

Figure 1: Two sample showers which we excluded from our analysis. In the case of the xi Draconid (XDR) shower (left), we were unable to detect a central peak in the data. In the case of the alpha Hydrid (AHY) shower (right), the apparent strength of the shower was comparable to the noise in the data.

such as an updated treatment of meteor trail length. The experimental pipeline can be used to generate fluxes from both the 29 MHz and 38 MHz observations. The limiting magnitude varies with transmitter frequency and power, but all fluxes are scaled to a constant limiting magnitude of +6.5.

2.1 Shower selection

Fluxes were measured for 80 showers that are apparent in the multi-station wavelet data. Flux values were calculated for each shower within the interval $[\lambda_{\min}, \lambda_0]$, where these minimum and maximum values were determined by adding a 5° buffer to the starting and ending solar longitudes published in Brown et al. (2010) for each shower. The Brown et al. (2010) interval is the period within which the shower produced a detectable wavelet enhancement over the background. One shower – the Quadrantids (QUAs) – has a manually adjusted interval, as the Brown et al. (2010) interval lasted far longer than the period over which the shower produced an apparent flux.

A default interval of one day is used for CMOR flux measurements. Finer time resolution is possible for the strongest showers under good observing conditions, but this is not possible for most of the showers considered here. Nevertheless, by combining many years of data, we can in some cases measure the peak time with less than 1-day resolution. We are unable to take this approach with infrequent or outbursting showers, and therefore exclude showers such as the October Draconids (DRAs) and Andromedids (ANDs) from this analysis.

Not all showers showed a clear central peak, and our initial parameter estimation (see section 5.1) failed for 32 showers. Visual inspection of the data confirmed that these cases showed no signs of a peak, and could not be improved by a manual initial parameter estimation. We present one such example in the left-hand panel of figure 1.

Out of the remaining 48 showers, 10 had signal amplitudes that were comparable to the scatter in the data. We again present an example in figure 1. Our confidence in the fits for these showers

would have been low, so we excluded them as well. That left us with the list of 38 showers for which we present fits in section 6.

2.2 Shower masking

The single-station shower identification method increases the probability of cross-contamination by other showers as well as by sporadic meteors. The detectable echoes originating from a given radiant are confined to a plane containing the radar station. Any two planes will have a line of intersection; echoes that lie along that line could arise from either shower. If the measured shower is weak and the competing shower is strong, this contamination may be significant.

CMOR's experimental flux pipeline addresses this issue by checking whether any major showers are active at the time of observation and, if so, excluding echoes that lie near the intersection of the two echo planes. We have opted to exclude this intersection region throughout the observation window. In one case, two major showers are active during the observation period for a minor shower; this minor shower is the sigma Serpentids (SSEs). Rather than further reduce the collection area with multiple masks, we mask the more clearly problematic shower (the QUAs). We then accept the possibility of contamination by the GEMs, although we see no signs of contamination at the nominal GEM peak.

3 Measurement uncertainty

CMOR's meteor flux algorithm is broadly described in Campbell-Brown (2004), but the algorithm is still being refined and there are discrepancies between the two pipelines (operational and experimental) and frequencies (29 and 38 MHz) that are not fully understood. Rather than wait an unknown amount of time for these discrepancies to be resolved, we instead use them to characterize the systematic uncertainty associated with the flux measurements. To our knowledge, no other attempt has been made to assess systematic uncertainty in radar meteor flux measurements.

3.1 Yearly variations

CMOR's flux measurements tend to run high in some years and low in others (see the top panel of figure 2 for an example). These variations have been ascribed to imperfectly accounted-for changes in observing conditions caused by equipment upgrades over the years (Campbell-Brown, 2019).

The yearly variations increase the degree of vertical scatter in the data and reduce the apparent significance of a peak in activity. Therefore, we decided to control for yearly variations in an empirical manner. Our approach is extremely simple: we calculated the geometric mean of every flux value for every recorded shower in a given year, and divided this by the geometric mean of all flux values over all years. These values are presented in the middle panel of figure 2. We then divide each year's shower fluxes by this quantity. This reduces the amount of scatter in the data that is caused by changes in observing conditions rather than by random noise in the data (see bottom panel of figure 2).

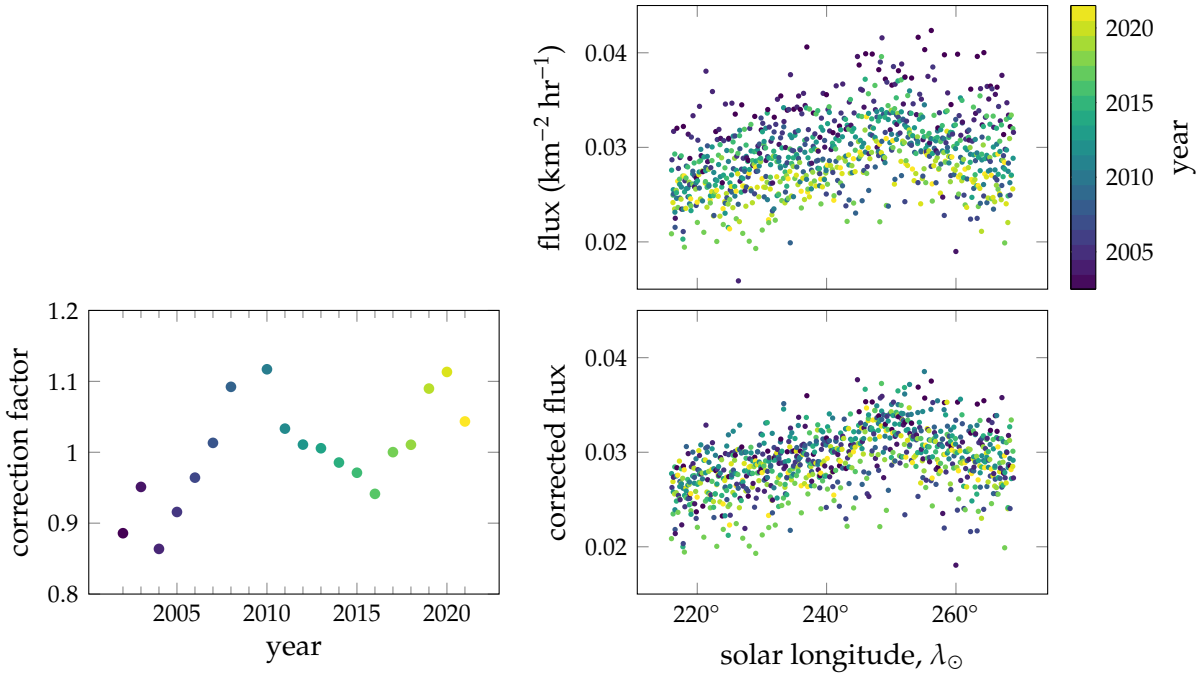

Figure 2: CMOR daily flux measurements for the November iota Draconid (NID) meteor shower, color-coded by year. We show the NID raw flux measurements (top), the yearly relative flux corrections for all showers (middle), and NID daily flux measurements with these corrections applied (bottom).

We have excluded the year 2009 from all analyses because we found that the fluxes from that year were poorly behaved compared to other years.

3.2 Systematic uncertainty

In this section, we compare meteor fluxes obtained using two different sets of observations (those from the 29 MHz receiver and those from the 38 MHz receiver) and two different versions of the CMOR flux pipeline (operational and experimental). 38 MHz fluxes are not available from the operational pipeline, and therefore any fluxes labeled "operational" are 29 MHz. Furthermore, the option to mask competing showers (see section 2.2) is only available in the experimental pipeline. We therefore turned off this option in the experimental pipeline in order to better compare the results with the operational pipeline. Finally, we derived and applied yearly correction factors (see section 3.1) for all three sets of flux data prior to comparing them. The top row of figure 3 shows the results. Before performing any further analysis, we excluded data points lying more than two standard deviations from the mean of each set. These outliers are identified in figure 3 using gray x's.

We supposed that the shower fluxes would likely differ between data sets by a multiplicative factor. However, it is possible for the background level to vary independently of this multiplicative factor if the 29 MHz and 38 MHz data have different limiting meteor magnitudes. We therefore fitted a linear relationship between the operational pipeline data and the 29 MHz, experimen-

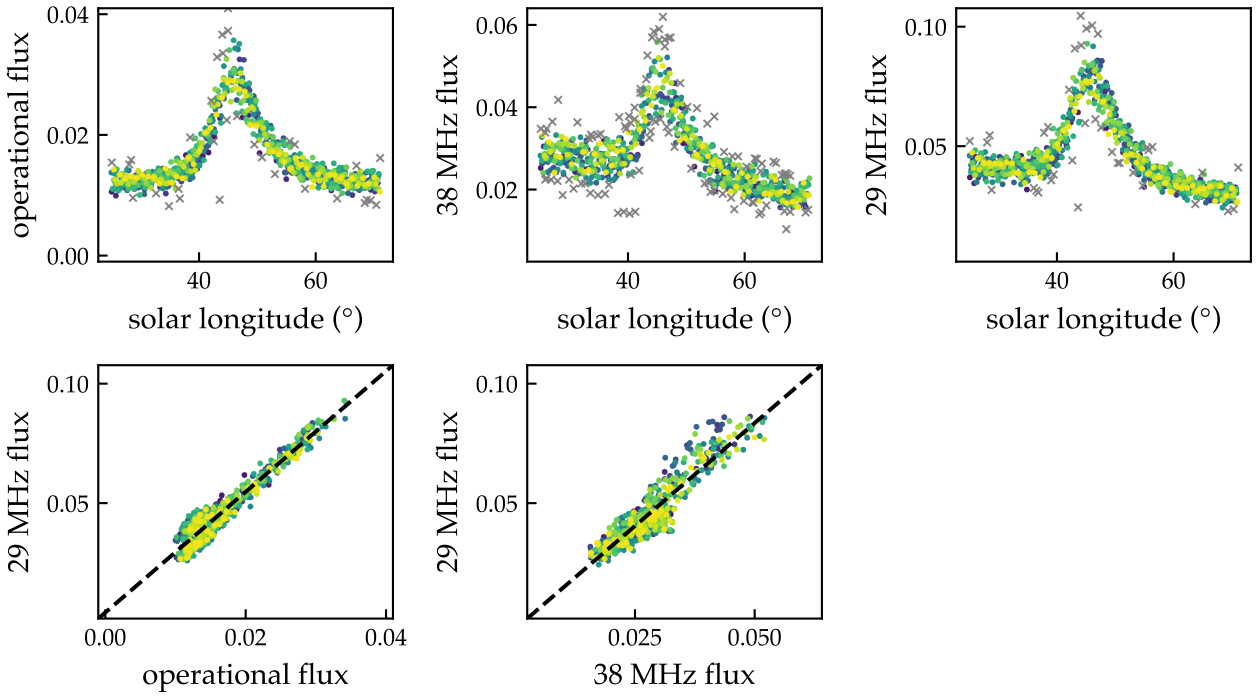

Figure 3: eta Aquariid (ETA) meteor flux measured using two different sets of observations (29 and 38 MHz) and two different versions of the flux pipeline (operational and experimental). Outliers are marked with gray x's and are excluded from the linear fits. The units of flux throughout this paper are km^{-2} hr^{-1}. Data are color-coded by year in the same manner as figure 2.

tal pipeline data and also between the 38 MHz and 29 MHz experimental pipeline data (bottom row of figure 3). The multiplicative factor will be the slope of this linear relationship, while any difference in background noise will be subsumed into the intercept.

Figure 3 illustrates this process for the ETA meteor shower; we then repeated this process for every meteor shower. Some showers have a very weak signal, as discussed in section 2.1; we excluded these showers by requiring that the variation in both the operational or 38 MHz data "explain" the majority of the variation the 29 MHz data (that is, we required that $R^2 > 0.5$ for both linear fits).

In general, we found that both the operational and 38 MHz fluxes were systematically lower than the 29 MHz fluxes. However, we do *not* assume that the average of the three fluxes is the best estimate of the true flux. Instead, we will assume that the flux ratios probe the scale of the systematic uncertainty. If we let

$$y = \ln(f_{\mathrm{op}}/f_{29}) \tag{1}$$

$$z = \ln(f_{38}/f_{29}) \tag{2}$$

then we can estimate the systematic uncertainty as follows

$$\hat{\sigma}_{\ln f} = \frac{2}{\sqrt{\pi}}\sqrt{\frac{y^2+z^2}{2}} \tag{3}$$

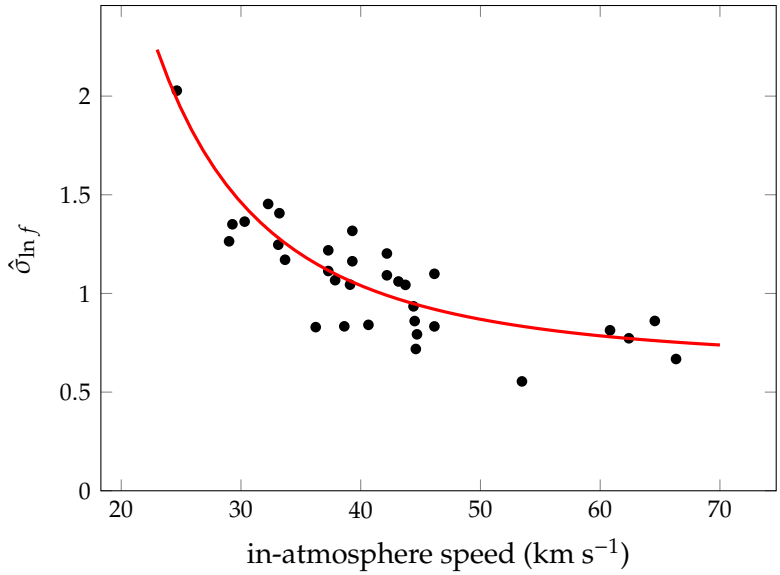

Figure 4: Estimated systematic uncertainty in the log of the flux as a function of the in-atmosphere velocity of a meteor shower. The red line represents equation 4.

where $2/\sqrt{\pi}$ is the bias correction for very small number statistics (Bolch, 1968). We are thus measuring the mean error about an assumed center at 0.

We find that the uncertainty is larger for slower showers (see figure 4). The overall trend appears to be:

$$\hat{\sigma}_{\ln f} \simeq 0.4 \left(\frac{v_{\text{atm}}}{40 \text{ km s}^{-1}} \right)^{-2.5} + 0.64 \tag{4}$$

where v_{atm} is the in-atmosphere speed of the shower. Thus, the uncertainty in the flux is at least a factor of $e^{0.64} \simeq 1.9$, and rises to a factor of $e^3 \simeq 20$ for $v_{\text{atm}} = 20$ km s^{-1}. We will adopt this equation as our estimate of the systematic uncertainty in the CMOR fluxes.

3.3 Random error

The CMOR flux pipeline does not include flux uncertainty estimates. It does include a tally of the number of meteors on which each flux measurement is based, n; we therefore initially tried an approach in which we assumed that flux (f) was proportional to n and uncertainty to $\sqrt{n}$, giving us $f/\sqrt{n}$ as an uncertainty estimate. However, this tends to produce smaller uncertainties on low flux measurements, which did not match the observed distribution. Instead, we noticed that the flux measurements for a particular shower tended to have a heavy left tail, with low values deviating more from the median than high values (see the top panel of figure 5).

So long as we have non-normal residuals, any fitting technique based on chi-square minimization will be invalid. We therefore decided to take an empirical approach towards estimating the flux uncertainties. We started by binning the data in 1-day (360°/365.25) increments: because fluxes are measured daily, each year contributes one measurement per bin (unless there was a

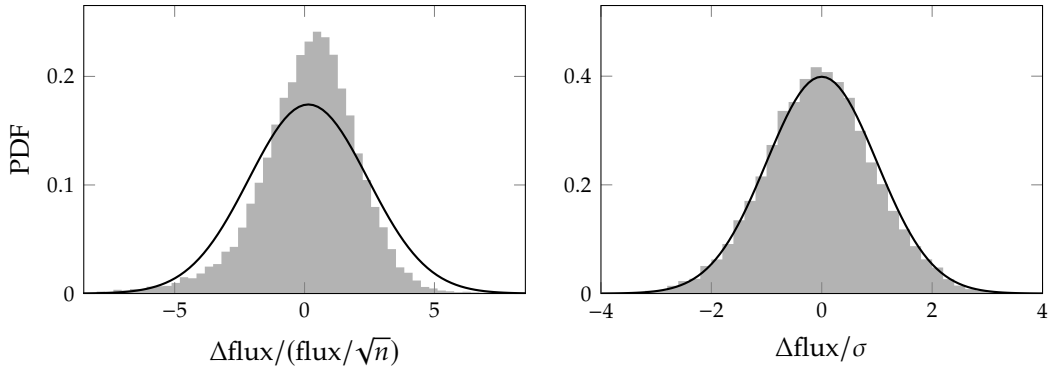

Figure 5: Studentized measurement dispersions using two uncertainty estimates. In the top panel, we use the flux divided by the square root of the number of observations. In the bottom panel, we use an empirical uncertainty estimate (equation 5). In both cases, we compare the distribution of values (gray histogram) with a normal distribution that has the same mean and standard deviation (black line).

lapse in observations). We then measured the sample mean and standard deviation of the flux per shower and bin (i.e., $\bar{f}_j$ and s_j for bin j).

We found that the following expression provides a residual distribution that is normal:

$$s_i = 0.32\, s_{j(i)} \left(\frac{n_{j(i)}}{n_i} \right)^{0.4} \tag{5}$$

When we normalize by these estimated uncertainties, the distributions of both our flux measurement dispersion (see figure 5) and fit residuals (see section 6) are normal.

3.4 Outliers

The flux data also include occasional outliers, some of which are wildly disparate from the rest of the data (see figure 6 for an example). To identify these, we once again make use of our binned data. We calculate the t-value corresponding to the difference between the average and an individual measurement:

$$t^* = \frac{f_i - \bar{f}_{j(i)}}{s_i} \tag{6}$$

We then use the modified Thompson tau test (Thompson, 1935; Pope, 1976) to compute the cut-off value for internally studentized residuals:

$$t_{\text{crit}} = \frac{m_j - 1}{\sqrt{m_j}} \frac{t_{m_j-2,\,1-\alpha/2}}{\sqrt{m_j - 2 + t^2_{m_j-2,\,1-\alpha/2}}} \tag{7}$$

where m_j is the number of flux measurements in bin j and α is our chosen confidence level. We have opted to set $\alpha = 0.5/i_{\text{max}}$; if there are no true outliers present, this choice should result in the exclusion of one non-outlier per shower approximately half the time.

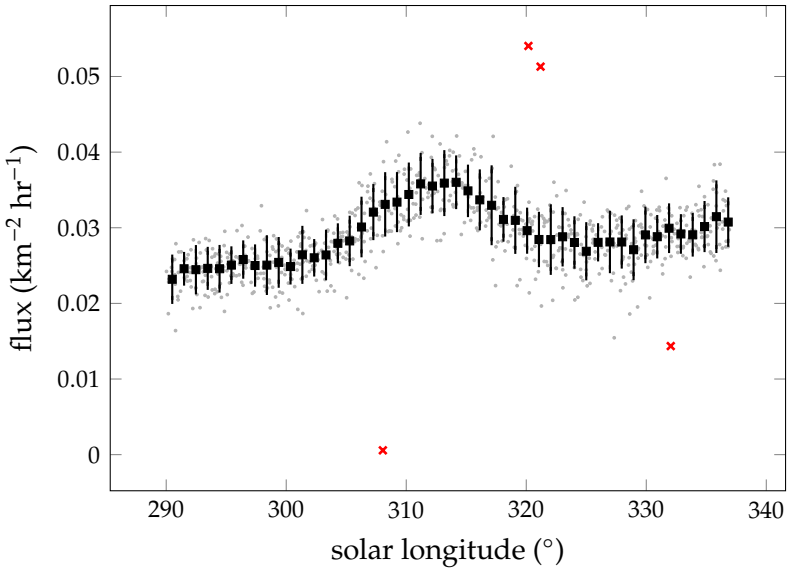

Figure 6: Flux measurements for the alpha Antliid (AAN) meteor shower. The average flux per day-length bin appears as larger black squares, with error bars that span ±1 standard deviation (*not* the standard deviation of the mean). The smaller points are individual flux measurements; the small gray points will be used to fit the activity profile, while the small red x marks indicate outliers.

If $|t^*| > t_{\text{crit}}$, we mark the point as an outlier and exclude it from our analysis. If there are multiple outliers in a bin, we discard the most extreme outlier and recalculate the t values before discarding any additional outliers. Figure 6 provides an example of this outlier identification as applied to the alpha Antliid (AAN) meteor shower.

4 Theoretical profile

The timing of non-variable meteor showers tends to remain the same year-to-year when measured in terms of solar longitude. Thus, solar longitude will be our predictor variable throughout this analysis, and the time of the peak, λ_{pk}, one of our fit parameters.

The Jenniskens (1994) profile is consistent with about half of the showers we examined. The remaining showers – including several stronger showers with a high signal-to-noise ratio – did not exhibit a sharp peak, and were better fit by an alternate profile that we describe in section 4.2.

In theory, one could obtain shape parameter estimates by performing a maximum likelihood estimation using this probability distribution function (PDF) and the solar longitudes of observed meteors belonging to a particular shower. In practice, raw meteor data are typically biased in a number of ways and observations do not carry equal "weight" in any calculation of flux or activity level. If the data are binned or averaged over some interval, it is useful to have a functional form for the cumulative distribution function (CDF) of our proposed distribution. We will therefore present the CDF for each proposed distribution; we will regress the 1-day difference in the CDF against the data (see section 5.2).

4.1 Asymmetric Laplace distribution

The profile used by Jenniskens (1994) and later adopted by McBride (1997), Moorhead et al. (2017), and Moorhead et al. (2019) takes the form of a double-exponential function:

$$\mathrm{ZHR} = \mathrm{ZHR}_0 \times \begin{cases} 10^{-B^+|\lambda_\odot - \lambda_0|} & \lambda_\odot < \lambda_0 \\ 10^{-B^-|\lambda_\odot - \lambda_0|} & \lambda_\odot \geq \lambda_0 \end{cases} \tag{8}$$

We find that the base-10 form leads to awkward factors of $\ln 10$ in the normalization, and opt to use the following equivalent function for an asymmetric Laplace distribution:

$$g(x) = \frac{ab}{a+b} \times \begin{cases} e^{+a(\lambda_\odot - \lambda_0)} & \lambda_\odot < \lambda_0 \\ e^{-b(\lambda_\odot - \lambda_0)} & \lambda_\odot \geq \lambda_0 \end{cases} \tag{9}$$

The corresponding cumulative distribution function (CDF) is:

$$G(x) = \begin{cases} \dfrac{b}{a+b} e^{+a(\lambda_\odot - \lambda_0)} & \lambda_\odot < \lambda_0 \\ 1 - \dfrac{a}{a+b} e^{-b(\lambda_\odot - \lambda_0)} & \lambda_\odot \geq \lambda_0 \end{cases} \tag{10}$$

4.2 Type IV generalized logistic distribution

When examining the data, we noticed that some showers exhibited a sharp peak while others had a much more rounded profile. We decided to construct a distribution that resembled the asymmetric Laplace distribution far from the peak, but had a "tunable" sharpness near the peak. We accomplished this by taking the power mean of two exponential functions:

$$g(x) \propto \left(e^{-a\,x/c} + e^{+b\,x/c} \right)^{-c} \tag{11}$$

where $x = \lambda_\odot - \lambda_0$ and the shape parameters a, b, and c are all positive. Note that when x is large and positive, $g(x) \sim \exp(-bx)$, and when x is large in magnitude and negative, $g(x) \sim \exp(+ax)$. Thus, the asymptotic behavior of equation (11) resembles that of an asymmetric Laplace distribution, but the shape of $g(x)$ near $x = 0$ is governed by the parameter c. Small values of c result in sharper peaks, while large values produce broad peaks; see figure 7 for an illustration.

This distribution can be re-arranged into the typical form of a Type IV generalized logistic distribution (GLD4; Prentice, 1976; Nassar and Elmasry, 2012):

$$g(y) = \frac{1}{B(c_a, c_b)} \frac{e^{-c_b y}}{(1+e^{-y})^{c_a + c_b}} \tag{12}$$

where $c_a = c\,a/(a+b)$, $c_b = c\,b/(a+b)$, and B is the complete beta function.

The CDF of type IV generalized logistic distribution (GLD4) is:

$$G(y) = \frac{1}{c_a\, B(c_a, c_b)} \frac{e^{-c_b y}}{(1+e^{-y})^{c_a + c_b}} e^{-c_b y} \tag{13}$$

$$\times\, {}_2F_1(1, 1-c_b; 1+c_a; -e^{y}) \tag{14}$$

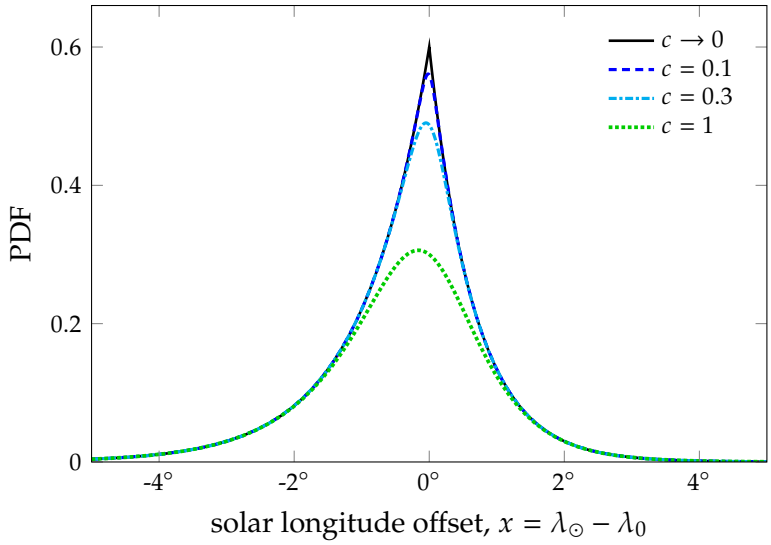

Figure 7: Non-normalized PDF of our custom distribution (eq. 11) for $a = 1$, $b = 1.5$, and four choices of c. The limiting case $c \to 0$ is equivalent to equation (9).

where ${}_2F_1$ is the ordinary or Gauss hypergeometric function.

It can be shown, using identity 15.10.E11 from the NIST Digital Library of Mathematical Functions,[2] that this expression is equivalent to:

$$G(z) = \frac{1}{c_a\, B(c_a, c_b)}\, z^{c_a}\, {}_2F_1(c_a, 1 - c_b; 1 + c_a; z), \text{ where} \tag{15}$$

$$z = \frac{1}{1 + e^{-y}} = \text{expit}(y) \tag{16}$$

This maps the interval $x \in (-\infty, \infty)$ to $z \in (0, 1)$. Note that we refer to the standard logistic function as "expit."

4.2.1 Alternate form and limiting behavior of CDF

While equation (15) fully specifies our CDF, we find that this formulation is not always adequate for numerical calculations. For instance, SciPy's `special.hyp2f1` function is implemented only for 64-bit floating point numbers, and, when $z \sim 1$, can produce large errors for some combinations of shower profile shape parameters. We therefore use equation 15 only for values of $\lambda < \lambda_0$, for which $x < 0$ and $z < \frac{1}{2}$.

For $z > \frac{1}{2}$, we follow the recommendation of Johansson (2019) and find an equivalent expression that takes $1 - z$ as its argument. To do so, we use identity 15.10.E21[3] to derive the following alternate form:

$$G(z) = 1 - \frac{z^{c_a}(1 - z)^{c_b}}{c_b\, B(c_a, c_b)}\, {}_2F_1(1, c, 1 + c_b; 1 - z) \tag{17}$$

[2] https://dlmf.nist.gov/15.10#E11
[3] https://dlmf.nist.gov/15.10#E21

Testing confirmed that this version was more reliable for $z > \frac{1}{2}$.

We found that, even armed with two formulations of our CDF, we were not quite able to proceed with our distribution fitting. In cases where the peak is sharp and c is small, exponentiating y often resulted in underflow or overflow errors within our data range. To minimize this effect, we substitute the limiting behavior of $G(z)$ for the CDF itself:

$$\lim_{z\to 0} {}_2F_1(c_a,\, 1-c_b,\, 1+c_a;\, z) = 1 + c_a \frac{1-c_b}{1+c_a} z \tag{18}$$

$$\lim_{z\to 1} {}_2F_1(1,\, c,\, 1+c_b;\, 1-z) = 1 + \frac{c}{1+c_b}(1-z) \tag{19}$$

4.2.2 Mode and curvature

Unlike the asymmetric Laplace distribution, our custom distribution does not necessarily peak at $x = 0$. Instead, the mode is located at:

$$x_{\text{pk}} = \lambda_{\text{pk}} - \lambda_0 - \frac{c}{a+b} \ln\left(\frac{b}{a}\right) \tag{20}$$

The peak is only located at $x = 0$ when $a = b$, as our PDF is undefined when $c = 0$. When interpreting our fit, we will need to recall that the time of peak activity is offset from λ_0 by this distance.

The curvature of the PDF at the mode quantifies the sharpness of the peak. If we differentiate equation 11 twice and set the location to x_{pk}, we obtain the following curvature:

$$g''(x_{\text{pk}}) = \frac{a^{1+c_a}\, b^{1+c_b}}{c\,(a+b)^c} \tag{21}$$

Thus, as $c \to 0$, the curvature $g''(x_{\text{pk}}) \to -\infty$ and $x_{\text{pk}} \to 0$, and the shape of our profile approaches that of an asymmetric Laplace distribution.

4.3 Asymmetry

Jenniskens (1994) found that most showers could be fit with a symmetric activity profile: that is, one in which the rise in activity prior to the peak takes place at the same rate as the decay after the peak. Both the Laplace and GLD4 PDFs are symmetric when $a = b$.

In order to make the degree of asymmetry clearer, we will fit for the following combinations of shape parameters:

$$k = \frac{1}{2}(b+a) \tag{22}$$

$$\ell = \frac{b-a}{b+a} \tag{23}$$

Thus, $k \in (0, \infty)$ is the average of a and b and describes the overall steepness of the activity profile, and $\ell \in (-1, 1)$ describes the asymmetry of the distribution.

4.4 Distribution truncation

The normalization of both distributions – asymmetric Laplace and GLD4 – assumes that the possible values of $\lambda_\odot$ range from $-\infty$ to $+\infty$. However, solar longitude is in fact limited to the range $[0, 360°]$ and, for a given shower, observations are usually limited to a far shorter interval.

Fortunately, having a closed form for the CDF of both distributions makes it simple to adjust the normalization for truncation. The truncated PDF and CDF can be calculated as:

$$g_{\text{trunc}}(x) = \frac{g(x)}{G(x_{\max}) - G(x_{\min})} \tag{24}$$

$$G_{\text{trunc}}(x) = \frac{G(x) - G(x_{\min})}{G(x_{\max}) - G(x_{\min})} \tag{25}$$

where $g(x)$ and $G(x)$ are the non-truncated PDF and CDF and the observations are limited to the interval $(x_{\min} \leq x \leq x_{\max})$.

4.5 Sporadic contamination

As discussed in section 2, our single-station meteor flux measurements are contaminated to a significant degree by the sporadic background. This contamination varies with both time (due to seasonal variations in the sporadic complex) and location in the sky (sporadic meteor radiants are concentrated into "sources"). Instead of attempting to subtract this background contamination from the data prior to analysis, we incorporate the background contribution into our model.

We adopt a fairly simple distribution for the background: we assume that the level of contamination varies linearly within the observation window. This corresponds to the following PDF:

$$g_{\text{bg}}(x) = \frac{1}{x_{\max} - x_{\min}} \left[1 + m \left(\frac{x - x_{\min}}{x_{\max} - x_{\min}} - \frac{1}{2} \right) \right] \tag{26}$$

The quantity $(x - x_{\min})/(x_{\max} - x_{\min})$ lies in the interval $[0, 1]$ and therefore $m \in [-2, 2]$. The corresponding CDF is:

$$G_{\text{bg}}(x) = \left(1 - \frac{m}{2} \right) \left(\frac{x - x_{\min}}{x_{\max} - x_{\min}} \right) + \frac{m}{2} \left(\frac{x - x_{\min}}{x_{\max} - x_{\min}} \right)^2 \tag{27}$$

Our observed flux distribution will be proportional to a linear combination of g_{bg} with that of our shower signal, g. We use γ to denote the fraction of the PDF that is associated with sporadic contamination:

$$g_{\text{tot}}(x) = (1 - \gamma)\, g(x) + \gamma\, g_{\text{bg}}(x) \tag{28}$$

We therefore must fit for m and γ in addition to x_0, k, ℓ (if allowing asymmetry), and c (if using the GLD4 distribution).

5 Fitting method

Before starting our fitting process, we transform all of our flux data, individual or binned, to a scale that is consistent with a PDF:

$$y_i = f_i/\rho,\ \bar{y}_j = \bar{f}_j/\rho \tag{29}$$

$$\rho = (\lambda_{\max} - \lambda_{\min}) \sum_j \bar{f}_j \tag{30}$$

where $\lambda_{\min}$ is the lower bound of our first solar longitude bin and $\lambda_{\max}$ is the upper bound of the last bin. This removes the amplitude from our fitting process; when complete, we can simply multiply our best fit by the denominator of equation (30) to convert back to flux.

5.1 Initial parameter estimate

We are fitting for a large number of parameters (up to six) simultaneously, and, possibly as a result, we find that many fitting algorithms struggle to converge on a solution unless provided with a good initial estimate. Through trial and error, we have devised a multi-step, iterative process for constructing this starting point.

Step 0: We construct our parameter estimate using the averaged data (i.e., $\bar{y}_j$). This will somewhat blunt the peak, but it greatly reduces noise.

We estimate λ_0 as the mid-point of the bin containing the maximum $\bar{y}_j$ value. This works as a starting point for the vast majority of cases, but we found we needed to provide manual estimates for a few showers with strong background trends: the alpha Capricornid (CAP), lambda Boötid (LBO), and Northern June Aquilid (NZC) meteor showers.

Step 1: We next estimate the quantity and slope of sporadic background contamination by performing linear regression on the data, using a weighting factor that emphasizes points that lie far from the peak:

$$w_j = \left(\frac{\lambda_j - \lambda_0}{\lambda_{\max} - \lambda_{\min}} \right)^2 \tag{31}$$

where λ_j is the midpoint of bin j. This obtains a reasonable estimate for the slope, but will overestimate the magnitude of the contamination (characterized via the intercept) because we have not yet separated the sporadic background from the shower signal (see the top panel of figure 8 for an example).

Before proceeding to the next step, we subtract the predicted values from the observed values to obtain the residuals, and adjust the location of our estimated peak to match that of the maximum *residual* rather than the maximum flux.

Step 2: In this step, we first perform a simple check as to whether a peak exists in the data. We select the largest interval that includes λ_1 and contains only positive residuals. We then run two Spearman rank tests for monotonicity (Virtanen et al., 2020; Zwillinger and Kokoska, 2000), one on the selected residuals preceding the peak and the second on the selected residuals after the peak.

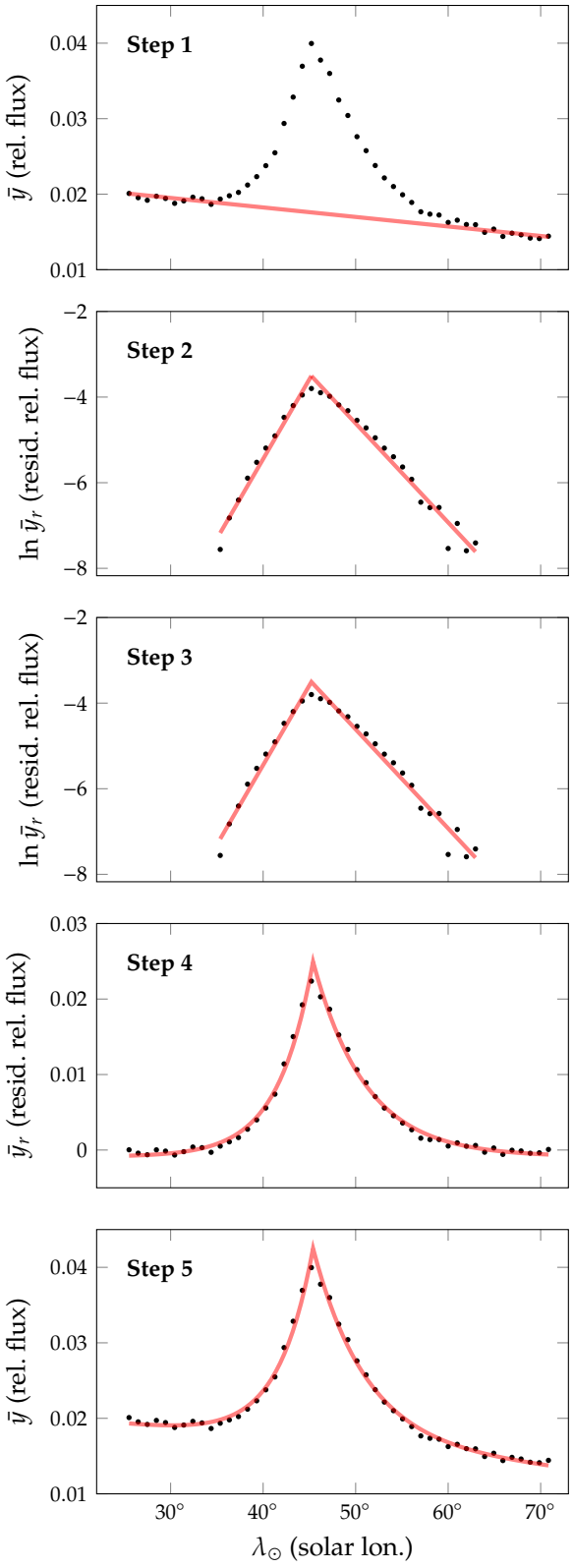

Figure 8: Our shape parameter estimation process, applied to eta Aquariid meteor shower relative fluxes that have been averaged over 20 years.

We require that both sets pass the test with a p-value less than 0.05, and that the rank correlation is positive prior to the peak and negative after the peak.

If the selected residuals pass both tests, we again use linear regression to estimate the shape parameters; see the second panel of figure 8 for an illustration. We obtain the slope and intercept relating the log of the residuals to the offset between solar longitude and the current best estimate of λ_0.

Step 3: We then average the intercept to obtain a common intercept and repeat the linear regression with the intercept fixed to refine our estimates of a and b. See the third panel of figure 8 for an illustration.

Step 4: Finally, we fit a double exponential function plus a vertical offset to the full set of residuals (see the fourth panel of figure 8).

Step 5: The results of Step 5, combined with the linear fit from Step 2, provide us with a full set of estimated shape parameters. The bottom panel of figure 8 compares this parameter estimate with the averaged data.

One could attempt to refine this estimate by iterating some or all of the above steps, but we find that the parameter estimates generated by a single pass through these steps provides a stable starting point for our distribution fitting.

5.2 Regression

In order to obtain an accurate fit, we use the 1-day difference in the CDF as our theoretical distribution rather than the PDF. Because the radar flux is measured over 1-day increments, this produces some natural rounding in the peak of the activity profile, which can be significant when fitting the double exponential profile to very brief showers such as the April Lyrids (LYR; see figure 9) and QUAs.

In an effort to minimize the covariance between fit parameters, we opted to fit for the peak solar longitude ($\lambda_{\rm pk}$) rather than the reference solar longitude of the distribution (λ_0). Thus, our fit parameters were the timing of peak activity, $\lambda_{\rm pk}$; the steepness of the distribution, k; the degree of asymmetry, ℓ; the smoothing parameter, c; the trend in the sporadic background contamination, m; and the fraction of background contamination, γ. The asymmetry parameter is omitted if the fit is constrained to be symmetric, and the smoothing parameter is omitted for a Laplace distribution.

We found that simple chi-square minimization worked well for both distributions. However, we also minimized a variant of the chi-squared statistic:

$$\chi^2_{\rm mod} = \chi^2 + 0.1 \left(\frac{\gamma - \gamma_0}{\sigma_y} \right)^2 \tag{32}$$

in which γ_0 is an estimate of the highest plausible level of sporadic background contamination and σ_y is a measure of the overall scatter about the best fit obtained by minimizing χ^2. We estimated γ_0 by averaging the endpoints of the distribution and adding $\frac{1}{2}\sigma$.

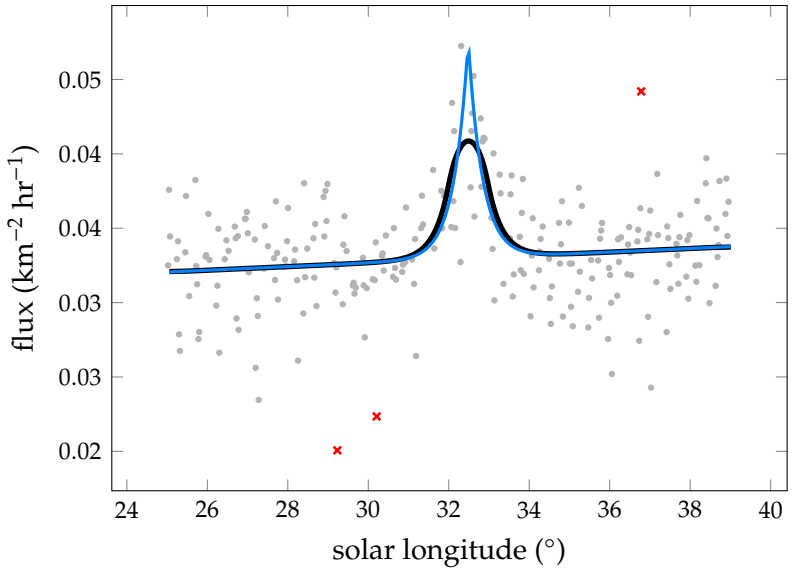

Figure 9: Flux measurements for the LYR meteor shower; red x's indicate outliers. We compare our best-fit curve (thick black line), in which we average the PDF over a 1-day interval to match the observation period, to the instantaneous PDF (blue line).

		minimized statistic	
distribution	asymmetry	χ^2	χ^2_{mod}
Laplace	$\ell = 0$	Ls1	Ls2
	$\ell \in (-1, 1)$	La1	La2
GLD	$\ell = 0$	Gs1	Gs2
	$\ell \in (-1, 1)$	Ga1	Ga2

Table 1: Four activity profile fitting combinations and their numbering.

For most showers, minimizing χ^2_{mod} produced fits that were very similar to those obtained by minimizing χ^2. Weak showers with a lower signal-to-noise ratio behaved differently; modifying χ^2 substantially increased the best-fit value of γ (see figure 10 for an example).

For each shower, we perform eight fits covering all possible combinations of theoretical profile (Laplace or GLD4), allowance for symmetry (symmetric or asymmetric), and minimization statistic (χ^2_{mod} or χ^2). We provide a numbering scheme for these eight fits in table 1.

5.3 Statistical tests

Chi-square minimization requires that our residuals be independent and normally distributed with equal variance. We perform a set of tests to verify whether these requirements are met. We also perform a chi-square goodness-of-fit test and verify whether the duration of detectable activity is compatible with multi-station shower observations.

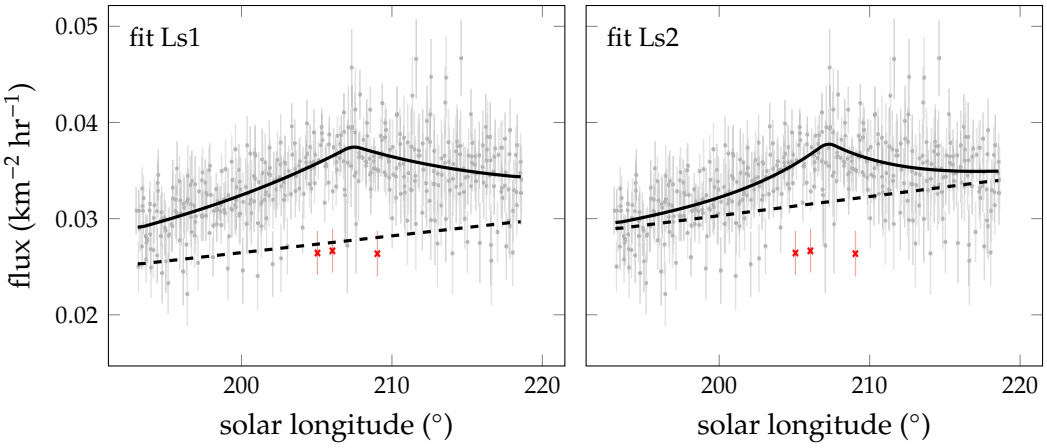

Figure 10: Flux measurements (points) for the alpha Ursae Majorid (AUM) meteor shower, estimated uncertainties (error bars), and best fit (black curve) and corresponding sporadic flux (dashed line). In the top panel, we have obtained our best fit by minimizing χ^2; in the bottom panel, we have minimized χ^2_{mod} (see equation 32).

5.3.1 Chi-square goodness-of-fit

The reduced chi-squared statistic is:

$$\chi^2_{\text{red}} = \frac{\chi^2}{\nu} \tag{33}$$

where the number of degrees of freedom is typically assumed to be $\nu = N - n_{\text{par}} - 1$ (see, e.g., Bevington et al., 1992). Since the expectation value of a chi-squared distribution is equal to the number of degrees of freedom, this value should be similar to unity. If $\chi^2_{\text{red}} \nsim 1$, this indicates either a poor fit or a poor characterization of the uncertainty (Bevington et al., 1992).

Rather than qualitatively assess the fit by examining the χ^2_{red} value, we perform a quantitative test using χ^2. We convert the test statistic to a right-tailed p-value by calculating the survival function of χ^2, assuming that it follows a chi-squared distribution with $N - n_{\text{par}} - 1$ degrees of freedom.

5.3.2 Signal plausibility

The flux data encompass a time interval that is wider than that over which the shower produces a detectable enhancement over the background as measured via a radiant-speed wavelet algorithm Brown et al. (2008, 2010). As a result, we expect the shower activity to be a small fraction of the total flux near the ends of the interval. We choose to make this expectation a requirement.

Specifically, we require that the shower enhancement be less than the noise level outside the window of detectability. We do not employ our flux uncertainty estimates for this comparison, as these vary from measurement to measurement depending on the number of meteor observations. Instead, we estimate the scatter as follows:

$$\hat{\sigma}^2_y = \frac{\sum_{i=1}^{N-1}(f_{i+1} - f_i)^2}{2(N-2)} \tag{34}$$

This formula is derived from the distribution of the difference of two independent and identically distributed normally variables, which is $\mathcal{N}(0, \frac{1}{2}\sigma^2)$. Our residuals are *not* normally distributed; equation (34) is intended to serve only as a rough estimate of the noise.

We then use our fits to find the predicted shower flux at $\lambda_{\min} + 5^\circ$ and $\lambda_{\max} - 5^\circ$ – that is, when activity first becomes detectable or becomes no longer detectable. If the shower-only flux at both times is less than $\hat{\sigma}_y$, we consider the shower to be have dropped to a level that is consistent with non-detection.

We do not necessarily expect that the flux exceeds $\hat{\sigma}_y$ *within* the Brown et al. (2010) intervals. Because the flux measurements are based on single-station data, it is more difficult to separate a shower from the sporadic background than it is when using multi-station trajectories. We therefore expect a lower signal-to-noise ratio, which means that a detectable wavelet signal may not translate to significantly elevated single-station fluxes. For the purposes of fitting, however, we do require that the estimated peak exceed 1.5 $\hat{\sigma}_y$.

5.3.3 Test for independence

We check whether our residuals are independent using an autocorrelation test. For this test, we once again bin our data; in this case, we calculate the mean residual value in one-day intervals. This choice is motivated by the fact that a poor fit should result in day-to-day and not year-to-year autocorrelations.

We then compute the Durbin-Watson test statistic (Durbin and Watson, 1950, 1951; Seabold and Perktold, 2010) on the mean residuals. Data are typically considered independent if this statistic, which can range from 0 to 4, has a value between 1 and 3. Some statisticians, however, recommend a range of 1.5 to 2.5 for a conclusion of no autocorrelation. The actual critical range for the Durbin-Watson statistic varies with the number of data points and the number of parameters, and is not straightforward to calculate (Seber and Lee, 2012).

We decided to bootstrap our way to a p-value. Our null hypothesis is that the residuals are uncorrelated and follow a normal distribution. We therefore drew 10,000 random samples of the same size as our binned mean residuals and calculated the Durbin-Watson test statistic for each sample. We used the distribution of simulated test statistic values to estimate the p-value corresponding to the test statistic of our residuals.

5.3.4 Test for equal variance

To test for equal variance, we used the Levene test (Virtanen et al., 2020; Levene, 1960). We decided to sort our residuals by the corresponding predicted response value and then divide them into groups of nearly equal size with a minimum sample size of 25.

Because our residuals should be normally distributed, we use Levene's original formulation in which deviations are measured relative to the group mean, rather than the alternative formulation of Brown and Forsythe (1974) that uses the group median.

We also test for autocorrelation in the residuals binned by predicted response value. The data should fail such a test if the value of the residuals varies with predicted value.

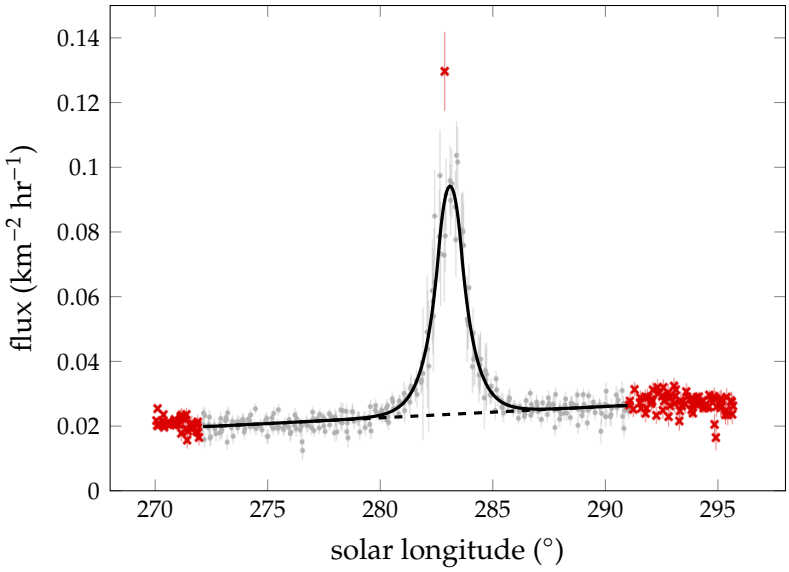

Figure 11: Flux measurements for the QUA meteor shower. Red "x" marks indicate outliers and excluded data.

5.3.5 Test for normality

Finally, we test the residuals for normality using a simple and commonly used statistical test (Virtanen et al., 2020; D'Agostino, 1971; D'Agostino and Pearson, 1973).

5.4 Interval trimming

In three cases, we found that a failed test was driven by anomalous behavior near one or both ends of the measurement interval. We were able to obtain better quality fits by trimming the interval over which we fit the data. For instance, the QUAs exhibit deviations from a linear background trend near the ends of the observation interval (see figure 11). Excluding the first and last few degrees results in a fit that passes all tests.

The three trimmed showers are the beta Equuleids (BEQs), for which we exclude observations after $\lambda_\odot = 120°$; the PERs, for which we exclude observations prior to $\lambda_\odot = 123°$; and the QUAs, for which we exclude observations prior to $\lambda_\odot = 272°$ and after $\lambda_\odot = 291°$.

6 Results

6.1 Sample results

We obtained at least partially successful fits for 38 radar-observable showers. Figure 12 shows sample results for the Southern delta Aquariids (SDAs). Similar sets of plots for all 38 showers are available in an appendix.

In the leftmost column of plots, the data appear in gray with the exception of outliers, which appear in red. The best fit is represented by the solid black line, while the dashed black line repre-

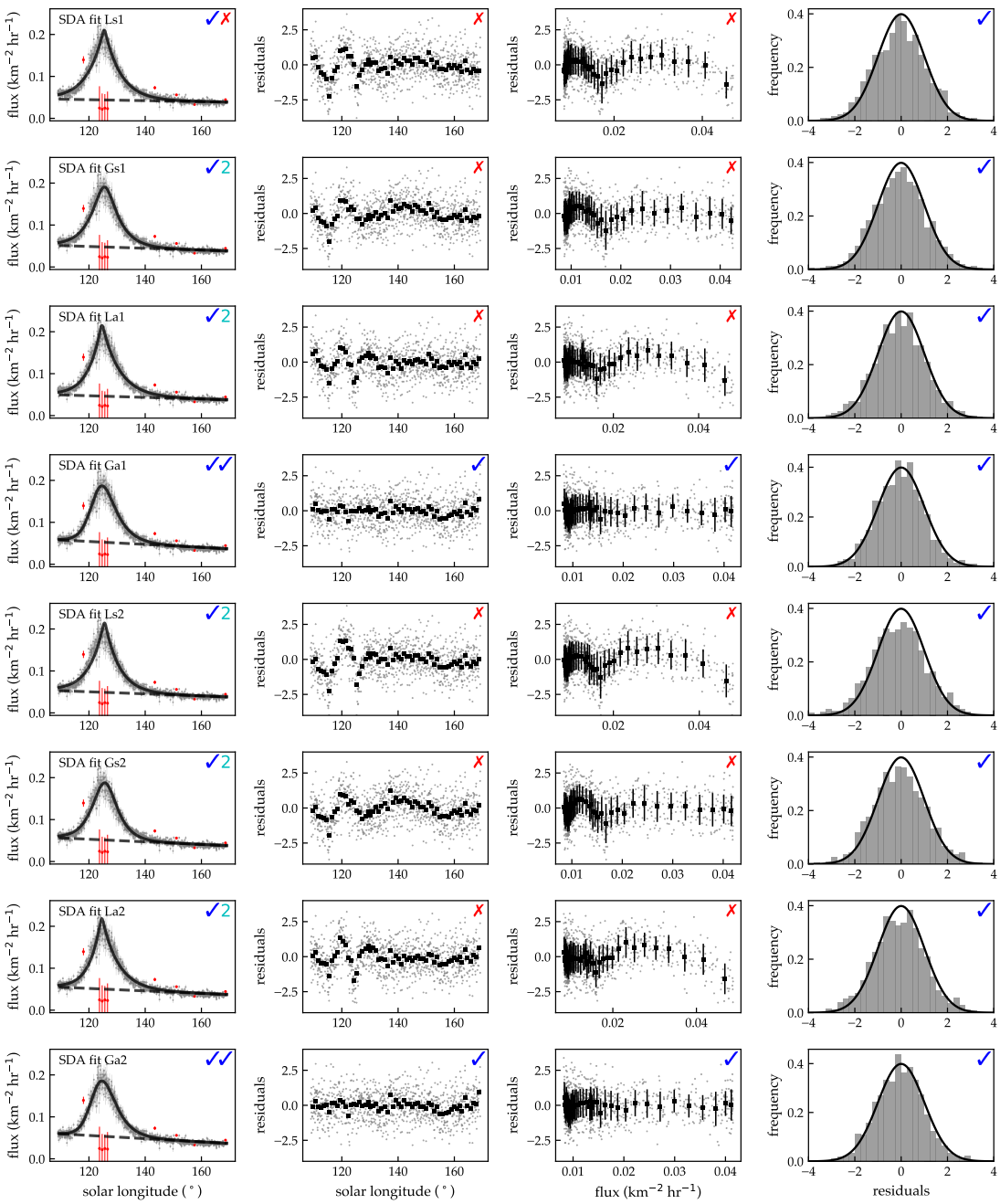

Figure 12: SDA meteor shower flux (left column) and residuals (remaining columns) for eight different fits (see table 1). Outliers appear in red. Checkmarks indicate that the fit passed a chi-squared goodness-of-fit test and signal plausibility test (first column), a Durbin-Watson test for independence (second column), another Durbin-Watson test for independence plus Levene's test for equal variances (third column), and a test for normality (last column). If the signal outside the reported shower activity period exceeded the scatter in the data by more than a factor of 1 but less than a factor of 2, we replace the second blue check mark in the first column of plots with a cyan "2."

sents the portion of the flux that is due to sporadic contamination. All plots in the left column are annotated with a blue checkmark or red "x" to indicate that the fits either pass or fail (respectively) a chi-squared goodness-of-fit test with a p-value greater than 0.01. A second blue checkmark indicates that the shower passed a test for signal plausibility. A cyan "2" indicates that it does not pass but is close to passing, and a red "x" indicates that it fails the signal plausibility test.

The second column of plots displays the studentized residuals vs. solar longitude:

$$\text{residual} = \frac{y_i - y_{\text{pred}}(x_i)}{s_i} \tag{35}$$

The individual residuals appear as small gray points, while the 1-day residual averages are shown as larger black squares. The checkmark or "x" indicates whether the averaged residuals pass a Durbin-Watson test for independence with a p-value greater than 0.01. In the case of the SDAs, only the asymmetric GLD4 distribution passes this test; this result is consistent with the visible fluctuations we see in the residuals of the Laplace and symmetric fits.

The third column of plots displays a "residuals vs. fits" plot; that is, it plots the studentized residuals against the values predicted by our fit. The individual residuals again appear in gray, while the prediction-binned residual averages appear as larger black squares. We depict the standard deviations of the binned residuals as error bars on the black squares. A checkmark indicates whether the averaged residuals pass both a Durbin-Watson test for independence and a Levene test for equal variance with a p-value greater than 0.01. If either test fails, we mark the plot with an "x."

Finally, the last column of plots shows the distribution of the studentized residuals. We overlay a standard normal distribution as a visual guide. The plots in this column all have blue checkmarks, indicating that they passed a test for normality with p-values greater than 0.01.

6.2 Fit selection

In some cases, exactly one of our eight fits satisfies all five tests described in section 5.3. In others, more than one of our fitting approaches (see table 1) produced a good match to the data. When choosing between multiple adequate fits, we always prioritize the simpler model: Laplace is preferred over GLD4, symmetry is preferred over asymmetry, and minimization of the chi-squared is preferred over minimization of the modified chi-squared. Thus, our most preferred fit is "Ls1," followed by "Gs1," and so on. Figure 12 and table 2 list the fits in order of decreasing preference.

Using our test results and this method ranking, we selected the best (or least bad) fit for each shower. These fits are presented in figures 13 and 14. Table 2 summarizes the full set of 1520 test results (i.e., every combination of 38 showers, 8 fit attempts, and 5 tests) and highlights our selected fits. There are several fit "tiers": in the first, the best fit unambiguously satisfies all test criteria. We highlight these cases in table 2 in green. In the second tier, highlighted in yellow, the best fit satisfies all but one criterion, and either (i) visual examination suggests that the test condition is not badly violated or (2) the shower flux outside the wavelet detection interval lies within 2 $\hat{\sigma}_y$ rather than 1 $\hat{\sigma}_y$. When conducting 1216 statistical tests with $\alpha = 0.01$ (we exclude our signal plausibility tests from this total as they do not have a defined level of significance), one would expect approximately 12 type I errors; thus, these five second-tier fits are *likely* to be valid, although we cannot prove it conclusively. In the third tier, highlighted in red, we were unable to

fit	Ls1					Gs1					La1					Ga1					Ls2					Gs2					La2					Ga2				
test	χ	s	x	y	n	χ	s	x	y	n	χ	s	x	y	n	χ	s	x	y	n	χ	s	x	y	n	χ	s	x	y	n	χ	s	x	y	n	χ	s	x	y	n
AAN	✓	✓		✓	✓	✓	✓	✓	✓	✓	✓	✓			✓	✓	✓	✓	✓	✓	✓	✓			✓	✓	✓	✓	✓	✓	✓	✓			✓	✓	✓	✓	✓
ARI	✓	✓			✓	✓	✓			✓	✓	2			✓	✓	✓		✓	✓	✓	✓			✓	✓	✓			✓	✓			✓	✓	✓		✓	✓
AUM	✓	2	✓	✓	✓	✓	2	✓	✓	✓	✓		✓	✓	✓	✓		✓	✓	✓	✓	✓	✓	✓	✓		✓	✓	✓	✓	✓	✓	✓	✓	✓	✓	✓	✓	✓
BEQ	✓		✓	✓	✓	✓		✓	✓	✓	✓		✓	✓	✓	✓		✓	✓	✓	✓		✓	✓	✓	✓		✓	✓	✓	✓		✓	✓	✓	✓		✓	✓
BTA	✓		✓	✓	✓	✓	2	✓	✓	✓	✓		✓	✓	✓	✓		✓	✓	✓	✓	✓	✓		✓	✓	✓	✓	✓	✓	✓			✓	✓	✓	✓	✓
CAP	✓	✓		✓	✓	✓	✓		✓	✓	✓	2	✓	✓	✓	✓	✓	✓	✓	✓	✓	✓		✓	✓	✓	✓		✓	✓	✓	✓	✓	✓	✓	✓	✓	✓	✓
DLT	✓		✓	✓	✓	✓		✓	✓	✓	✓		✓	✓	✓	✓		✓	✓	✓	✓	2		✓	✓	✓	✓	✓	✓	✓	✓		✓	✓	✓	✓		✓	✓
DSX	✓	2		✓	✓	✓	✓		✓	✓	✓	✓		✓	✓	✓	✓	✓	✓	✓	✓	✓	✓		✓	✓	✓	✓		✓	✓	✓	✓	✓	✓	✓	✓	✓	✓	✓
EPG	✓		✓	✓	✓	✓		✓	✓	✓	✓		✓	✓	✓	✓		✓	✓	✓	✓		✓	✓	✓	✓		✓	✓	✓	✓		✓	✓	✓	✓		✓	✓
ETA	✓	✓		✓	✓	✓	✓		✓	✓	✓	✓	✓	✓	✓	✓	✓	✓	✓	✓	✓	✓		✓	✓	✓	✓		✓	✓	✓	✓	✓	✓	✓	✓	✓	✓	✓
GEM	✓	✓			✓	✓	✓			✓	✓	✓			✓	✓	✓			✓	✓	✓			✓	✓	✓			✓	✓			✓	✓	✓			✓
GUM	✓	2	✓	✓	✓	✓	✓	✓	✓	✓	✓		✓	✓	✓	✓		✓	✓	✓	✓	✓	✓	✓	✓	✓	✓	✓	✓	✓	✓	2	✓	✓	✓	✓	✓	✓
JLE	✓	✓	✓	✓	✓	✓	✓	✓	✓	✓	✓	✓	✓	✓	✓	✓	✓	✓	✓	✓	✓	✓	✓	✓	✓	✓	✓	✓	✓	✓	✓	✓	✓	✓	✓	✓	✓	✓	✓
KLE	✓		✓	✓	✓	✓		✓	✓	✓	✓		✓	✓	✓	✓		✓	✓	✓	✓	✓		✓	✓	✓	✓	✓	✓	✓	✓		✓	✓	✓	✓		✓	✓
LBO	✓		✓	✓	✓	✓		✓	✓	✓	✓		✓	✓	✓	✓		✓	✓	✓	✓		✓	✓	✓	✓		✓	✓	✓	✓		✓	✓	✓	✓		✓	✓
LDR	✓	✓	✓	✓	✓	✓	✓	✓	✓		✓		✓	✓		✓		✓	✓		✓	✓	✓	✓	✓	✓	✓	✓	✓		✓	✓	✓	✓	✓	✓	2		
LLY	✓	✓	✓	✓	✓	✓	✓	✓	✓	✓	✓	2	✓	✓	✓	✓	2	✓	✓	✓	✓	✓	✓	✓	✓	✓	✓	✓	✓	✓	✓	✓	✓	✓	✓	✓	✓	✓
LMI	✓	✓	✓	✓	✓	✓	✓	✓	✓	✓	✓	✓	✓	✓	✓	✓	✓	✓	✓	✓	✓	✓	✓	✓	✓	✓	✓	✓	✓	✓	✓	✓	✓	✓	✓	✓	✓	✓	✓
LYR	✓	✓	✓	✓	✓	✓	✓	✓	✓	✓	✓	✓	✓	✓	✓	✓	✓	✓	✓	✓	✓	✓	✓	✓	✓	✓	✓	✓	✓	✓	✓	✓	✓	✓	✓	✓	✓	✓	✓
NID	✓	2	✓	✓	✓	✓	2	✓	✓	✓	✓	✓	✓	✓	✓	✓	✓	✓	✓	✓	✓	✓	✓	✓	✓	✓	✓	✓	✓	✓	✓	✓	✓	✓	✓	✓	✓	✓	✓
NOC	✓		✓	✓	✓	✓		✓	✓	✓	✓		✓	✓	✓	✓	✓	✓	✓	✓	✓	✓		✓	✓	✓	✓		✓	✓	✓		✓	✓	✓	✓		✓	✓
NOO	✓		✓	✓	✓	✓		✓	✓	✓	✓	2	✓	✓	✓	✓	2	✓	✓	✓	✓	2		✓	✓	✓	2		✓	✓	✓		✓	✓	✓	✓		✓	✓
NZC	✓					✓		✓	✓	✓	✓					✓		✓		✓	✓	2		✓	✓	✓		✓	✓	2		✓	✓	✓	✓		✓	✓
OCE	✓	✓				✓	✓		✓		✓	✓				✓	✓	✓	✓		✓	✓				✓	✓				✓	✓			✓	✓	✓		✓	
ORI	✓	✓	✓	✓		✓	✓	✓	✓		✓	✓	✓	✓		✓	✓	✓	✓		✓	✓	✓	✓		✓	✓	✓	✓		✓	✓	✓	✓		✓	✓	✓	✓	
PCA	✓				✓	✓				✓	✓	2	✓	✓	✓		2	✓	✓	✓	✓	2		✓	✓	✓	✓		✓	✓	✓	✓	✓	✓	✓	✓	✓	✓	✓
PER	✓	✓	✓		✓	✓	✓	✓		✓	✓	✓	✓	✓	✓	✓	✓	✓	✓	✓	✓	✓	✓	✓	✓	✓	✓	✓	✓	✓	✓	✓	✓	✓	✓	✓	✓	✓	✓
QUA	✓	✓	✓	✓	✓	✓	✓	✓	✓	✓	✓	✓	✓	✓	✓	✓	✓	✓	✓	✓	✓	✓	✓	✓	✓	✓	✓	✓	✓	✓	✓	✓	✓	✓	✓	✓	✓	✓	✓
SDA	✓			✓		✓	2		✓		✓	2			✓	✓	✓	✓	✓	✓	✓	2			✓	✓	2			✓	2			✓	✓	✓	✓	✓	✓
SMA	✓		✓	✓	✓	✓	✓	✓	✓	✓	✓		✓	✓	✓	✓		✓	✓	✓	✓	✓	✓	✓	✓	✓	✓	✓	✓	✓	✓	✓	✓	✓	✓	✓	✓	✓	✓
SSE	✓	✓	✓	✓	✓	✓	✓	✓	✓	✓	✓	2	✓	✓	✓	✓	✓	✓	✓	✓	✓	✓	✓		✓	✓	✓	✓	✓	✓	✓	✓	✓	✓	✓	✓	✓	✓	✓
STA	✓			✓	✓	✓	✓	✓	✓	✓	✓			✓	✓	✓	2	✓	✓	✓	✓	✓			✓	✓	✓	✓	✓	✓	✓	✓			✓	✓	✓		✓
SZC	✓	✓	✓	✓	✓	✓	✓	✓	✓	✓	✓	2	✓	✓	✓	✓	✓	✓	✓	✓	✓	✓	✓	✓	✓	✓	✓	✓	✓	✓	✓	2	✓	✓	✓	✓	✓	✓	✓
TCB	✓	2		✓	✓	✓	✓	✓	✓	✓	✓	2		✓	✓	✓	✓	✓	✓	✓	✓	✓			✓	✓	✓	✓	✓	✓	✓	2		✓	✓	✓	✓	✓	✓
URS	✓	✓	✓	✓	✓	✓	✓	✓	✓	✓	✓	✓	✓	✓	✓	✓	✓	✓	✓	✓	✓	✓	✓	✓	✓	✓	✓	✓	✓	✓	✓	✓	✓	✓	✓	✓	✓	✓	✓
XCB	✓	2	✓	✓	✓	✓	✓	✓	✓	✓	✓	2	✓	✓	✓	✓	✓	✓	✓	✓	✓	✓	✓		✓	✓	✓	✓	✓	✓	✓	✓		✓	✓	✓	✓	✓	✓
XSA	✓		✓	✓	✓	✓		✓	✓	✓	✓		✓	✓	✓	✓		✓	✓	✓	✓	✓	✓	✓	✓	✓	✓	✓	✓	✓	✓	✓	✓	✓	✓	✓	✓	✓	✓
ZPE	✓		✓	✓	✓	✓		✓	✓	✓	✓		✓	✓	✓	✓		✓	✓	✓	✓	2	✓	✓	✓	✓		✓	✓	✓	✓		✓	✓	✓	✓	✓	✓	✓

Table 2: Statistical test results for our four fit attempts (see table 1) for each shower.

χ : chi-squared goodness-of-fit
s : signal plausibility
x : residuals independent when ordered by x
y : residuals independent with equal variance when ordered by y
n : residuals are normally distributed

✓ : test passed with $p > 0.01$ or signal $< \hat{\sigma}_y$ outside active interval
i : visual inspection suggests test is not badly violated
2 : signal $< 2\hat{\sigma}_y$ outside active interval

find a good fit candidate, and simply identify what appears to be the least bad option. We include these 6 third-tier fits because they may still be useful for providing a rough description of the shower activity profile.

We would like to note that multiple good fits are not an indication that the fit is underconstrained. Because the asymmetric Laplace distribution corresponds to the limiting behavior of the GLD4 distribution as $c \to 0$, any shower that can be fit by the former can also be fit by the latter. Indeed, we can see from table 2 that this is the case. Similarly, any shower that can be fit by a symmetric distribution can also be fit by an "asymmetric" distribution in which $\ell \sim 0$. Furthermore, our modified chi-squared (eq. 32) is designed to deviate from the actual chi-squared statistic by a very small quantity. In most cases, it makes little difference in the final fit. This is the intended behavior: it should modify the fit only for showers with lower signal-to-noise ratios.

6.3 Peak flux

In table 3, we provide the fit parameters as well as peak time and flux. We compute the instantaneous peak flux using the PDF rather than the 1-day difference in CDF that describes the data. For broad showers, the two values do not differ much, but the peak PDF value may lie noticeably above the maximum measurement for brief showers. The peak flux does not include the sporadic component.

The reader may notice that four showers – the LBOs, xi Coronae Borealids (XCBs), Southern Daytime omega Cetids (OCEs), and Daytime zeta Perseids (ZPEs) – do not have finite uncertainties on at least one parameter. In most cases, this parameter is c and the uncertainty could not be estimated because the minimum chi-square occurred at the upper end of our allowed range in c. Larger values of c resulted in computational errors without visibly improving the fit.

In figure 15, we present showers in order of decreasing peak flux to illustrate which showers produce the most significant fluxes. Unsurprisingly, the GEMs appear at the top, followed by several other major showers: the SDAs, QUAs, ARIs, and ETAs. However, we find that a couple of comparatively obscure showers – the Southern June Aquilids (SZCs) and theta Coronae Borealids (TCBs) – compete with major showers such as the Orionids (ORIs), URSs, and PERs. This is partly due to the fact that CMOR sees relatively weak ORI and PER activity, possibly because of a lack of small particles in these streams.

Figure 15 also illustrates the impact of our estimated systematic uncertainty. In the left panel, labeled "low," the flux values have been reduced by one $\sigma_{\ln f}$; that is, the flux has been multiplied by $e^{-\sigma_{\ln f}}$. After applying this transformation, the showers no longer appear in strictly decreasing order; this is because $\sigma_{\ln f}$ is a function of shower speed. In the right panel, labeled "high," the flux values have been increased by one $\sigma_{\ln f}$.

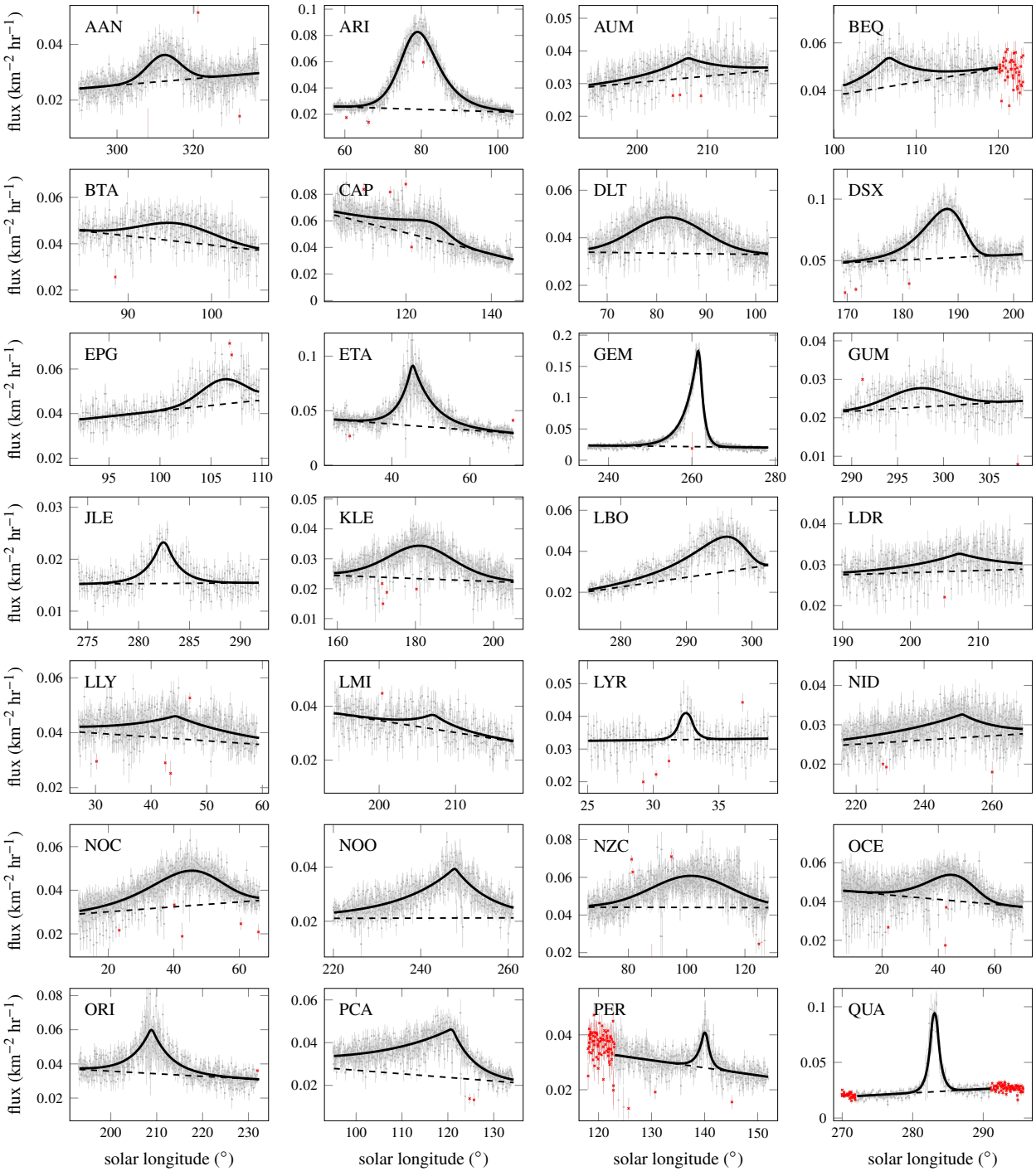

Figure 13: Flux measurements (points), estimated uncertainties (error bars), and our best fit for the activity profile (solid black curve) for 28 out of 38 meteor showers. Outliers and excluded data appear in red, and we display the sporadic background portion of our best fit as a dashed line.

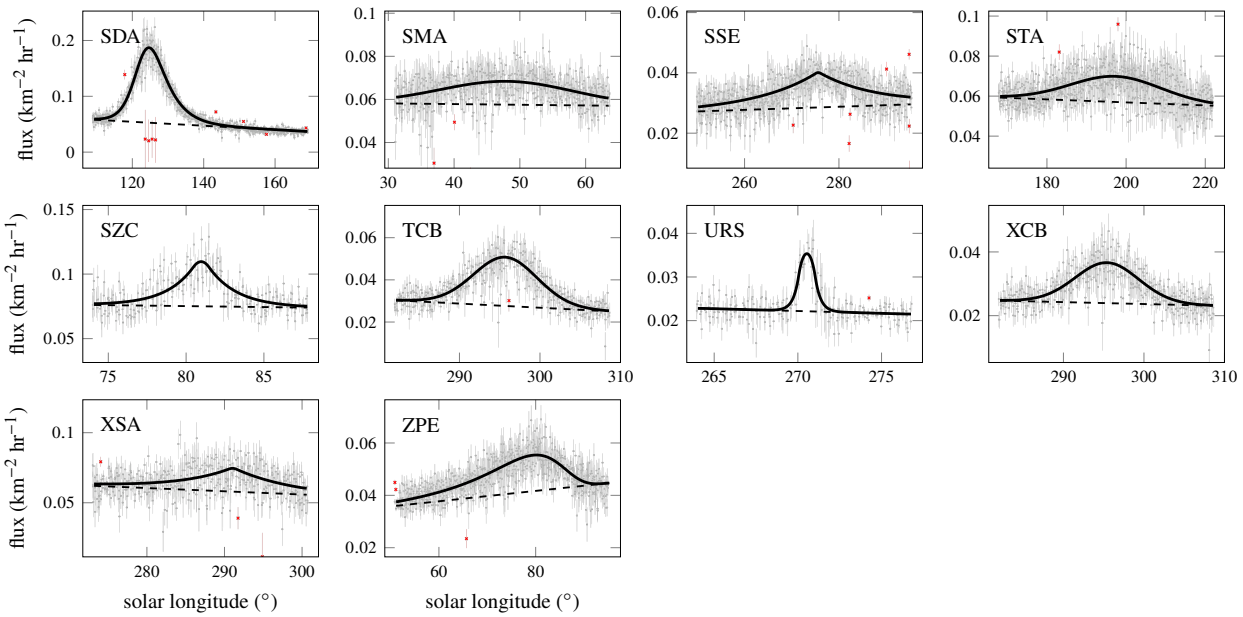

Figure 14: Flux measurements (points), estimated uncertainties (error bars), and our best fit for the activity profile (solid black curve) for the remaining 10 out of 38 meteor showers. Outliers appear in red, and we display the sporadic background portion of our best fit as a dashed line.

	SNR	fit	λ_0 (deg)	k	ℓ	c	λ_{pk} (deg)	f_{pk} (km^{-2} yr^{-1})
AAN	2.9	Gs1	312.25 ± 0.18	1.204 ± 0.025		27.30 ± 0.52	312.25 ± 0.19	0.009 47 ± 0.000 76
ARI	15.2	Ga1	77.51 ± 0.27	0.282 ± 0.018	−0.276 ± 0.026	1.51 ± 0.24	79.026 ± 0.080	0.0590 ± 0.0043
AUM	1.9	Ls2	207.19 ± 0.30	0.166 ± 0.028			207.19 ± 0.30	0.006 24 ± 0.000 66
BEQ	2.8	Ls2	106.63 ± 0.19	0.236 ± 0.034			106.63 ± 0.19	0.0127 ± 0.0014
BTA	1.6	Gs2	95.846 ± 0.091	1.09 ± 0.26		23.3 ± 11.3	95.85 ± 0.46	0.007 77 ± 0.000 84
CAP	2.1	Ga1	129.61 ± 0.92	0.33 ± 0.38	0.76 ± 0.17	1.5 ± 2.9	125.25 ± 0.66	0.0127 ± 0.0022
DLT	3.7	Gs2	82.41 ± 0.24	0.696 ± 0.019		25.39 ± 0.78	82.41 ± 0.24	0.0151 ± 0.0012
DSX	6.3	Ga1	194.3 ± 1.3	1.4 ± 2.0	0.81 ± 0.25	7.8 ± 14.0	187.98 ± 0.13	0.0399 ± 0.0094
EPG	2.7	Gs2	106.267 ± 0.062	2.33 ± 0.17		26.9 ± 2.6	106.27 ± 0.16	0.0112 ± 0.0013
ETA	10.0	La1	45.26 ± 0.13	0.2484 ± 0.0092	−0.229 ± 0.029		45.26 ± 0.13	0.0583 ± 0.0044
GEM	39.3	La1	261.724 ± 0.044	0.644 ± 0.015	0.503 ± 0.013		261.724 ± 0.044	0.172 ± 0.013
GUM	1.8	Gs1	297.328 ± 0.056	1.45 ± 0.41		23.5 ± 12.2	297.33 ± 0.31	0.004 95 ± 0.000 52
JLE	4.4	Ls1	282.431 ± 0.069	0.695 ± 0.080			282.431 ± 0.069	0.009 35 ± 0.000 89
KLE	3.5	Gs2	181.29 ± 0.11	0.208 ± 0.065		2.9 ± 2.1	181.29 ± 0.25	0.0110 ± 0.0011
LBO	4.1	Ga1	306.1743 ± 0.0028	6.3 ± ∞	0.97 ± 0.76	30.0 ± ∞	295.80 ± 0.24	0.0171 ± 0.0037
LDR	1.6	Ls1	207.19 ± 0.58	0.124 ± 0.076			207.19 ± 0.58	0.0044 ± 0.0016
LLY	2.1	Ls1	44.41 ± 0.46	0.085 ± 0.046			44.41 ± 0.46	0.0083 ± 0.0025
LMI	1.4	Ls1	207.08 ± 0.36	0.30 ± 0.12			207.08 ± 0.36	0.0056 ± 0.0011
LYR	2.8	Ls1	32.484 ± 0.068	2.30 ± 0.55			32.484 ± 0.068	0.0136 ± 0.0027
NID	2.2	La1	251.28 ± 0.84	0.066 ± 0.028	0.36 ± 0.21		251.28 ± 0.84	0.0060 ± 0.0012
NOC	3.8	Ga1	56.7 ± 3.3	0.24 ± 0.51	0.56 ± 0.61	4.6 ± 14.7	44.68 ± 0.33	0.0160 ± 0.0039
NOO	5.2	La1	247.80 ± 0.33	0.099 ± 0.018	0.208 ± 0.095		247.80 ± 0.33	0.0185 ± 0.0019
NZC	3.4	Gs2	101.57 ± 0.41	0.345 ± 0.020		22.3 ± 2.4	101.57 ± 0.40	0.0168 ± 0.0013
OCE	2.5	Ga1	75.033 ± 0.015	1.3 ± 10.6	0.86 ± 1.00	30.0 ± ∞	45.08 ± 0.37	0.0133 ± 0.0011
ORI	5.2	Ls1	208.85 ± 0.12	0.239 ± 0.016		27	208.85 ± 0.12	0.0270 ± 0.0022
PCA	6.0	La1	120.97 ± 0.20	0.135 ± 0.012	0.603 ± 0.048		120.97 ± 0.20	0.0231 ± 0.0018
PER	4.1	La1	140.13 ± 0.13	1.05 ± 0.13	0.20 ± 0.12		140.13 ± 0.13	0.0162 ± 0.0018

QUA	19.5	Ls1	283.098	± 0.031	1.582	±	0.069						283.098	± 0.031	0.1016	± 0.0083
SDA	15.6	Ga1	123.10	± 0.36	0.321	±	0.027	−0.321	± 0.035	1.51	±	0.29	124.673	± 0.079	0.1347	± 0.0099
SMA	1.7	Gs1	47.960	± 0.070	0.43	±	0.77			18.9	±	65.5	48.0	± 1.3	0.0108	± 0.0039
SSE	2.9	Ls1	275.59	± 0.28	0.081	±	0.016						275.59	± 0.28	0.0118	± 0.0012
STA	1.7	Gs1	197.314	± 0.049	0.38	±	0.57			18.5	±	55.5	197.31	± 0.70	0.0128	± 0.0024
SZC	4.2	Ls1	80.97	± 0.10	0.549	±	0.088						80.97	± 0.10	0.0395	± 0.0039
TCB	4.6	Gs1	295.6839	± 0.0095	0.9	±	1.9			13.9	±	57.5	295.68	± 0.12	0.023	± 0.013
URS	5.5	Ls1	270.541	± 0.049	3.04	±	0.64						270.541	± 0.049	0.0255	± 0.0046
XCB	3.3	Gs1	295.3998	± 0.0060	1.1	±	3.3			17.5	±	∞	295.40	± 0.16	0.0127	± 0.0050
XSA	1.7	Ls2	291.08	± 0.42	0.142	±	0.025						291.08	± 0.42	0.0172	± 0.0020
ZPE	3.3	Ga2	100.3205	± 0.0063	2.9	±	26.9	0.97	± 0.29	30.0	±	∞	79.43	± 0.37	0.0138	± 0.0011

Table 3: Best fit distribution parameters (λ_0, k, and, where applicable, ℓ and c) and the corresponding peak solar longitude and flux (λ_{pk} and f_{pk}). We have sorted the showers in order of decreasing peak flux.

28

1 / 2	s	a
L	10 / 2	5 / 0
G	6 / 3	5 / 1

Table 4: The number of activity profiles that fall into each category: (L)aplacian vs. (G)LD4, (s)ymmetric vs. (a)symmetric, and minimizing the (1) unmodified vs. the (2) modified chi-squared statistic (eq. 32).

6.4 Correlations and trends

We conducted several simple statistical tests for trends or correlations in our results. For all statistical tests, we exclude the third-tier (or "bad") fits, leaving us with a sample size of $n = 32$ first- and second-tier fits. First, we performed a chi-square test for independence on the $2 \times 2 \times 2$ array of the number of showers that fall into each fit category (see table 4); we found no evidence of any correlation. Thus, GLD4 fits are not more likely to be asymmetric, fits using a modified chi-squared statistic ("2") are not more likely to be consistent with a Laplace distribution, and so forth.

Next, we measured the proportion of GLD4 and asymmetric fits. Based on our first- and second-tier results, we find that a GLD4 distribution fits the data better than a Laplace distribution about half the time (with a point estimate of 47% and a 95% confidence interval of 29%–65%). Similarly, we find that an asymmetric distribution fits the data better an estimated 34% of the time (with a 95% confidence interval of 19–53%).

We also find that biasing the fit towards a higher sporadic contamination level (i.e., minimizing a modified chi-squared statistic) is sometimes (about $\sim 20\%$ of the time) able to bring the shower signal to within 1-2 σ of the background level outside of the expected window of observability.

Finally, we conducted tests to determine whether our fit categories were correlated with shower duration or amplitude. Our goal is to determine whether there are any signs of one fit type being associated with a poorer temporal resolution or weaker signal. Rather than use the wavelet durations from Brown et al. (2010), we measured the duration over which the shower component of our best or chosen fit was at least 1 $\hat{\sigma}_y$ in amplitude.

We tested the influence of duration and signal strength by performing a simple t-test for a difference in mean duration or mean signal strength between fit groups (see figure 16). We found no significant difference in peak signal strength ($f_{\mathrm{pk}}/\hat{\sigma}_y$) with fit type, but we found that, when we group Laplace and GLD4 fits together, asymmetric fits corresponded to significantly longer durations (p-value = 0.001). This indicates that finer temporal sampling may be needed to determine whether the activity profiles of brief showers are symmetric or asymmetric in shape.

6.5 Future work

We are able to *approximate* the shape of the GEM and ARI activity profiles with our chosen distributions, but the residuals indicate that neither an asymmetric Laplace distribution nor a GLD4 distribution fully capture the shape of these profiles. A superposition of distributions, as proposed by Jenniskens (1994), may be more successful. The GEMs are a particularly interesting case

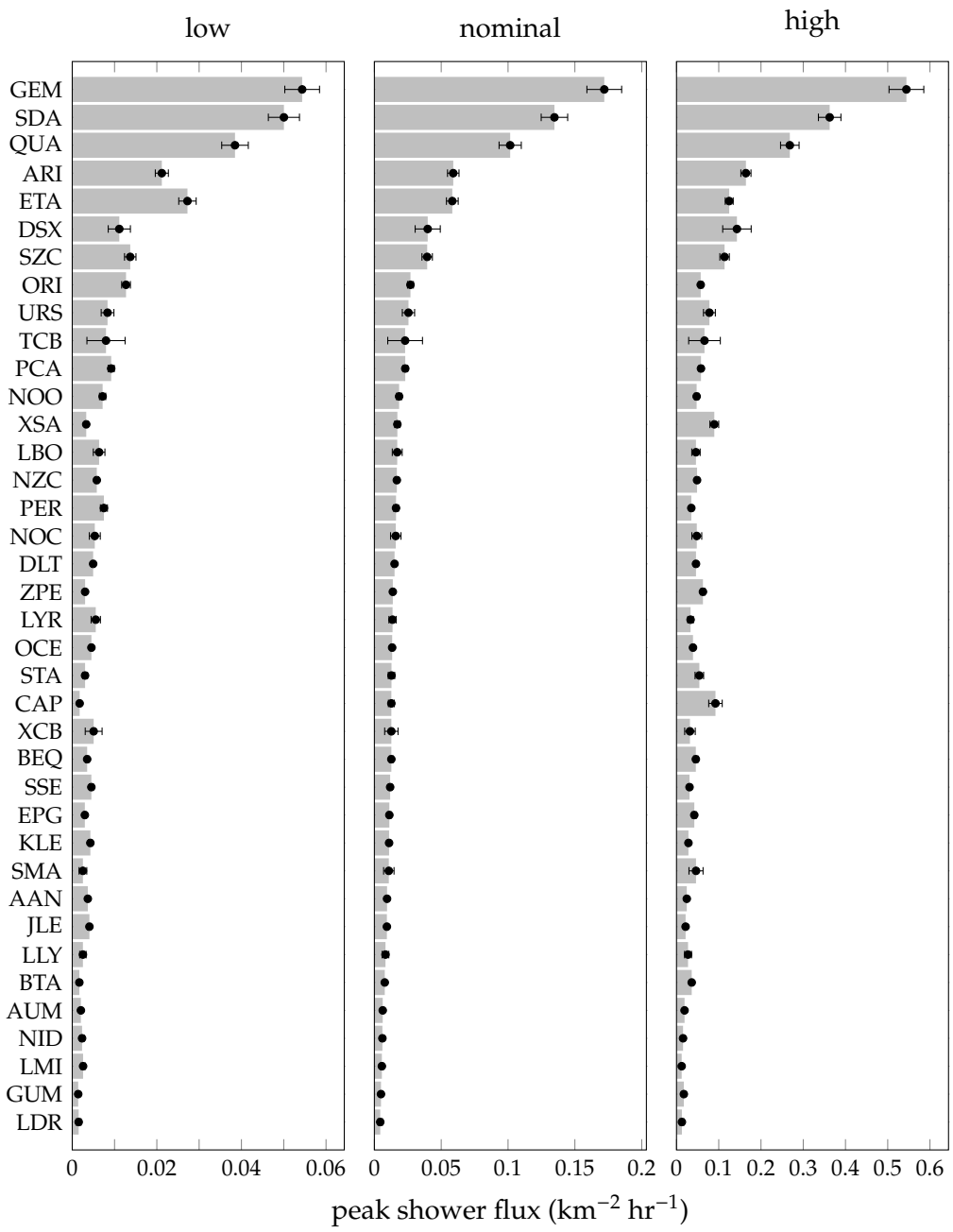

Figure 15: The full list of showers we fit, sorted in order of descending peak flux (center). The peak flux is depicted by the gray bars/black points, with error bars corresponding to the uncertainties provided in table 3. The left panel shows the results when reduced by one $\sigma_{\ln f}$, and the right panel shows the results when increased by one $\sigma_{\ln f}$.

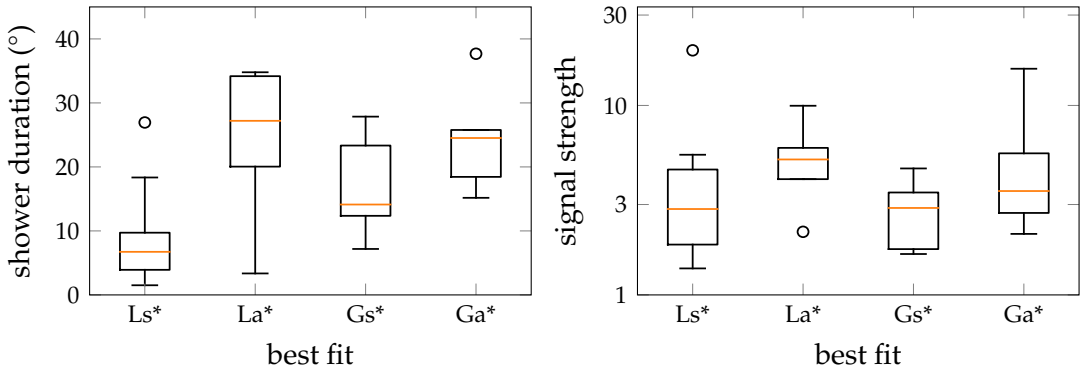

Figure 16: Box plots of shower duration (left) and signal strength (right); we have divided the showers into four groups by best fit type. The asterisk indicates that, for example, fit types Ls1 and Ls2 have been combined into a single category. Showers that are better fit by an asymmetric distribution (La* and Ga*) tend to have longer durations on average.

for further study because their duration is known to vary with particle size (Olsson-Steel, 1987; Šimek and McIntosh, 1989).

The TCB, and, to a lesser extent, the XCB and LBO showers produce relatively large peak fluxes. These three showers have similar radiants, speeds, and are active at similar times; according to Brown et al. (2008), the XCB and TCB showers have identical active intervals. The LBO shower occurs a little earlier but has a 10-day overlap with the XCB and TCB active period. If we were to combine these three showers, their flux could rival the ARIs in strength. However, the high apparent LBO flux at the end of its activity window could be due in part to TCB and XCB contamination. We suggest a careful joint characterization of these three showers as a possible area of future work.

7 Conclusion

We have conducted a detailed characterization of 38 meteor shower activity profiles using single-station flux data from the the Canadian Meteor Orbit Radar (CMOR). Our profiles differ from previously published profiles in that we allow for a blunted or rounded peak in the flux; we accomplish this using a type IV generalized logistic distribution (GLD4). We choose the best fit for each shower using a battery of statistical tests that ensure that all requirements of regression fitting are met.

Overall, we find that half of showers are better fit with a GLD4 distribution than a Laplace distribution, and that one-third of showers are better fit with an asymmetric distribution. Furthermore, showers that have a longer interval of detectability are more likely to be better fit by an asymmetric distribution, hinting that finer sampling of brief showers might result in additional asymmetric fits.

A crucial part of our fitting process is that we fit for a sporadic contamination component. In fact, we (weakly) bias the results in favor of a high contamination fraction if it results in a more plausible signal-to-noise ratio. Without this sporadic contamination component, we would

severely overestimate the flux of weaker showers. The gamma Ursae Minorids (GUMs), for instance, account for only 18% of the total flux passing through its echo plane at the time of peak activity.

Allowing for GLD4 fits also reduces the tendency to overestimate the peak flux of showers with broad peaks. For instance, fitting the Southern delta Aquariids (SDAs) with a Laplace rather than a GLD4 distribution results in a peak flux that is 25% higher (and is a noticeably worse fit; see figure 12).

Our careful fitting process and subtraction of sporadic contamination allow us to better compare the relative strengths of showers. Figure 15 ranks all fitted showers by their peak flux; the ten strongest showers are the Geminids (GEMs), SDAs, Quadrantids (QUAs), Daytime Arietids (ARIs), eta Aquariids (ETAs), Daytime Sextantids (DSXs), Southern June Aquilids (SZCs), Orionids (ORIs), Ursids (URSs), theta Coronae Borealids (TCBs).

This report also estimates the algorithm uncertainty associated with CMOR flux measurements by comparing three different sets of flux measurements. It appears that the uncertainty is a factor of two for showers with high speeds, but can be significantly more uncertain for low-speed meteor showers.

Funding information

This work was supported in part by NASA Cooperative Agreement 80NSSC21M0073 and by the Natural Sciences and Engineering Research Council of Canada.

References

Bevington, P. R., Robinson, D. K., and Bunce, G., 1992. *Data Reduction and Error Analysis for the Physical Sciences*. WCB/McGraw-Hill, Boston, Mass., 2nd edition. ISBN: 978-0-07-911243-9.

Bolch, B. W., 1968. The teacher's corner: More on unbiased estimation of the standard deviation. *The American Statistician*, 22(3):27. DOI: 10.1080/00031305.1968.10480476.

Brown, M. B. and Forsythe, A. B., 1974. Robust tests for the equality of variances. *Journal of the American Statistical Association*, 69:364–367.

Brown, P. and Weryk, R. J., 2020. Coordinated optical and radar measurements of low velocity meteors. *Icarus*, 352:113975. DOI: 10.1016/j.icarus.2020.113975.

Brown, P., Weryk, R. J., Wong, D. K., and Jones, J., 2008. A meteoroid stream survey using the Canadian Meteor Orbit Radar. I. Methodology and radiant catalogue. *Icarus*, 195(1):317–339. DOI: 10.1016/j.icarus.2007.12.002.

Brown, P., Wong, D. K., Weryk, R. J., and Wiegert, P., 2010. A meteoroid stream survey using the Canadian Meteor Orbit Radar. II: Identification of minor showers using a 3D wavelet transform. *Icarus*, 207(1):66–81. DOI: 10.1016/j.icarus.2009.11.015.

Campbell-Brown, M. D., 2004. Radar observations of the Arietids. *MNRAS*, 352(4):1421–1425. DOI: 10.1111/j.1365-2966.2004.08039.x.

Campbell-Brown, M. D., 2019. Solar cycle variation in radar meteor rates. *MNRAS*, 485(3): 4446–4453. DOI: 10.1093/mnras/stz697.

Cervera, M. A., Elford, W. G., and Steel, D. I., 1997. A new method for the measurement of meteor speeds: The pre-t_0 phase technique. *Radio Science*, 32(2):805–816. DOI: 10.1029/96RS03638.

Cook, A. F. A working list of meteor streams. In *Proceedings of IAU Colloq. 13, "Evolutionary And Physical Properties Of Meteoroids"*, pages 183–191. NASA SP-319, 1973. URL: https://ntrs.nasa.gov/citations/19740011323.

D'Agostino, R., 1971. An omnibus test of normality for moderate and large sample sizes. *Biometrika*, 58(34):341–348. DOI: 10.1093/biomet/58.2.341.

D'Agostino, R. and Pearson, E. S., 1973. Tests for departure from normality. Empirical results for the distributions of b_2 and $\sqrt{b}$. *Biometrika*, 60(3):613–622. DOI: 10.1093/biomet/60.3.613.

Durbin, J. and Watson, G. S., 1950. Testing for serial correlation in least squares regression: I. *Biometrika*, 37(3/4):409–428. DOI: 10.1093/biomet/37.3-4.409.

Durbin, J. and Watson, G. S., 1951. Testing for serial correlation in least squares regression: II. *Biometrika*, 38(1-2):159–178. DOI: 10.1093/biomet/38.1-2.159.

Egal, A., Wiegert, P., Brown, P. G., Campbell-Brown, M., and Vida, D., 2020. Modeling the past and future activity of the Halleyid meteor showers. *Astronomy & Astrophysics*, 642:A120. DOI: 10.1051/0004-6361/202038953.

Jenniskens, P., 1994. Meteor stream activity I. The annual streams. *Astronomy & Astrophysics*, 287: 990–1013.

Jenniskens, P., Nénon, Q., Albers, J., Gural, P. S., Haberman, B., Holman, D., Morales, R., Grigsby, B. J., Samuels, D., and Johannink, C., 2016. The established meteor showers as observed by CAMS. *Icarus*, 266:331–354. DOI: 10.1016/j.icarus.2015.09.013.

Jenniskens, P., Lyytinen, E., and Baggaley, J., 2020. An outburst of delta Pavonids and the orbit of parent comet C/1907 G_1 (Grigg-Mellish). *Planetary and Space Science*, 189:104979. DOI: 10.1016/j.pss.2020.104979.

Johansson, F., 2019. Computing hypergeometric functions rigorously. *ACM Transactions on Mathematical Software*, 45(3):30. DOI: 10.1145/3328732.

Jones, J. and Morton, J. D., 1977. The determination of meteor stream radiants from single station observations. *Bulletin of the Astronomical Institutes of Czechoslovakia*, 28:267. URL: https://ui.adsabs.harvard.edu/abs/1977BAICz..28..267J.

Jones, J., Brown, P., Ellis, K. J., Webster, A. R., Campbell-Brown, M., Krzemenski, Z., and Weryk, R. J., 2005. The Canadian Meteor Orbit Radar: System overview and preliminary results. *Planetary & Space Science*, 53(4):413–421. DOI: 10.1016/j.pss.2004.11.002.

Levene, H. Robust tests for equality of variances. In *Contributions to Probability and Statistics: Essays in Honor of Harold Hotelling*, pages 278–292. Stanford University Press, 1960.

McBride, N., 1997. The importance of the annual meteoroid streams to spacecraft and their detectors. *Advances in Space Research*, 20(8):1513–1516. DOI: 10.1016/S0273-1177(97)00428-6.

Molau, S. and Rendtel, J., 2009. A comprehensive list of meteor showers obtained from 10 years of observations with the IMO Video Meteor Network. *WGN, Journal of the IMO*, 37(4):98–121. URL: https://ui.adsabs.harvard.edu/abs/2009JIMO...37...98M.

Molau, S., Crivello, S., Goncalves, R., Saraiva, C., Stomeo, E., Strunk, J., and Kac, J., 2019. Results of the IMO Video Meteor Network - October 2018. *WGN, Journal of the IMO*, 47(6):188–192. URL: https://ui.adsabs.harvard.edu/abs/2019JIMO...47..188M.

Moorhead, A. V., Cooke, W. J., and Campbell-Brown, M. D. Meteor shower forecasting for spacecraft operations. In *Proceedings of the 7th European Conference on Space Debris*. ESA Space Debris Office, 2017.
URL: https://conference.sdo.esoc.esa.int/proceedings/sdc7/paper/77/SDC7-paper77.pdf.

Moorhead, A. V., Egal, A., Brown, P. G., Moser, D. E., and Cooke, W. J., 2019. Meteor shower forecasting in near-Earth space. *Journal of Spacecraft and Rockets*, 56:1531–1545.
DOI: 10.2514/1.A34416.

Moorhead, A. V., Clements, T., and Vida, D., 2021. Meteor shower radiant dispersions in Global Meteor Network data. *MNRAS*, 508(1):326–339. DOI: 10.1093/mnras/stab2557.

Nassar, M. M. and Elmasry, A., 2012. A study of generalized logistic distributions. *Journal of the Egyptian Mathematical Society*, 20(2):126–133. DOI: 10.1016/j.joems.2012.08.011.

Ogawa, H. and Steyaert, C., 2017. Major and daytime meteor showers using Global Radio Meteor Observations covering the period 2001-2016. *WGN, Journal of the IMO*, 45(5):98–106.
URL: https://ui.adsabs.harvard.edu/abs/2017JIMO...45...98O.

Olsson-Steel, D., 1987. The dispersal of the Geminid meteoroid stream by radiative effects. *MNRAS*, 226:1–17. DOI: 10.1093/mnras/226.1.1.

Pope, A. J., 1976. The Statistics of Residuals and the Detection of Outliers. NOAA Technical Report NOS 65 NGS 1. URL: https://www.ngs.noaa.gov/PUBS_LIB/TRNOS65NGS1.pdf.

Prentice, R. L., 1976. A generalization of the probit and logit methods for dose response curves. *Biometrics*, 32(4):761–768. DOI: 10.2307/2529262.

Seabold, S. and Perktold, J. Statsmodels: Econometric and statistical modeling with Python. In *Proceedings of the 9th Python in Science Conference (SciPy 2010)*, pages 92–96, 2010.
DOI: 10.25080/Majora-92bf1922-011.

Seber, G. A. F. and Lee, A. J., 2012. *Linear Regression Analysis*. Wiley, Hoboken, N.J., 2nd edition. ISBN: 978-0-471-41540-4.

Šimek, M. and McIntosh, B. A., 1989. Geminid meteor stream: Activity as a function of particle size. *Bulletin of the Astronomical Institutes of Czechoslovakia*, 40:288–298. URL: https://ui.adsabs.harvard.edu/abs/1989BAICz..40..288S.

SonotaCo, 2009. A meteor shower catalog based on video observations in 2007-2008. *WGN, Journal of the IMO*, 37(2):55–62. URL: https://ui.adsabs.harvard.edu/abs/2009JIMO...37...55S.

Thompson, W. R., 1935. On a criterion for the rejection of observations and the distribution of the ratio of deviation to sample standard deviation. *The Annals of Mathematical Statistics*, 6(4): 214–219. DOI: 10.1214/aoms/1177732567.

Virtanen, P., Gommers, R., Oliphant, T. E., Haberland, M., Reddy, T., Cournapeau, D., Burovski, E., Peterson, P., Weckesser, W., Bright, J., van der Walt, S. J., Brett, M., Wilson, J., Millman, K. J., Mayorov, N., Nelson, A. R. J., Jones, E., Kern, R., Larson, E., Carey, C. J., Polat, İ., Feng, Y., Moore, E. W., VanderPlas, J., Laxalde, D., Perktold, J., Cimrman, R., Henriksen, I., Quintero, E. A., Harris, C. R., Archibald, A. M., Ribeiro, A. H., Pedregosa, F., van Mulbregt, P., and SciPy 1.0 Contributors, 2020. SciPy 1.0: Fundamental algorithms for scientific computing in Python. *Nature Methods*, 17:261–272. DOI: 10.1038/s41592-019-0686-2.

Webster, A. R., Brown, P. G., Jones, J., Ellis, K. J., and Campbell-Brown, M., 2004. Canadian Meteor Orbit Radar (CMOR). *Atmospheric Chemistry & Physics*, 4(3):679–684. DOI: 10.5194/acp-4-679-2004.

Younger, J. P., Reid, I. M., Li, G., Ning, B., and Hu, L., 2015. Observations of the new Camelopardalids meteor shower using a 38.9 MHz radar at Mohe, China. *Icarus*, 253:25–30. DOI: 10.1016/j.icarus.2015.02.021.

Zwillinger, D. and Kokoska, S., 2000. *CRC Standard Probability and Statistics Tables and Formulae*. Chapman & Hall, New York, N.Y. ISBN: 978-1-58488-059-2.